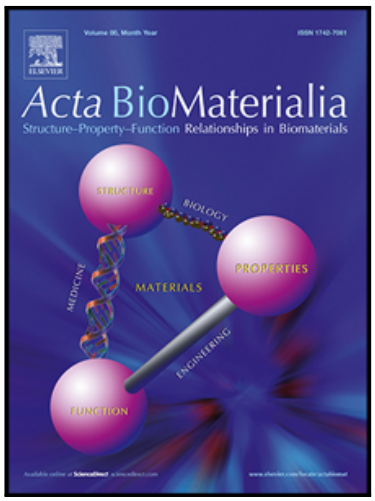

Insights from Molecular Dynamics into bactericidal mechanisms of copper and carbon substrates using reactive force field potential

Caaisha Warsame , Jonathan Joseph Bean , Hamed Rajabi , Jaya Verma , Martyna Michalska , Saurav Goel

PII: S1742-7061(26)00002-4
DOI: https://doi.org/10.1016/j.actbio.2026.01.002
Reference: ACTBIO 10483

To appear in: *Acta Biomaterialia*

Received date: 19 August 2025
Revised date: 10 December 2025
Accepted date: 2 January 2026

Please cite this article as: Caaisha Warsame , Jonathan Joseph Bean , Hamed Rajabi , Jaya Verma , Martyna Michalska , Saurav Goel , Insights from Molecular Dynamics into bactericidal mechanisms of copper and carbon substrates using reactive force field potential, *Acta Biomaterialia* (2026), doi: https://doi.org/10.1016/j.actbio.2026.01.002

Insights from Molecular Dynamics into bactericidal mechanisms of copper and carbon substrates using reactive force field potential

Caaisha Warsame[1], Jonathan Joseph Bean[1,2], Hamed Rajabi[1], Jaya Verma[1], Martyna Michalska[3,4] and Saurav Goel[1, 5*]

[1] School of Engineering and Design, London South Bank University, London, SE1 0 AA, UK
[2] MatNex, 145 City Road, London EC1V 1AZ, UK
[3] Manufacturing Futures Lab, University College London, London, E20 2AE, UK
[4] Department of Mechanical Engineering, University College London, London, WC1E 7JE, UK
[5] Department of Mechanical Engineering, University of Petroleum and Energy Studies, Dehradun, 248007, India

**Corresponding author: goels@lsbu.ac.uk*

Abstract

Reactive Force Field (ReaxFF) molecular dynamics (MD) simulations, which allow dynamic bond formation and charge transfer, were conducted to investigate the incipient bactericidal/bacteriostatic activity of copper (Cu) and carbon (C) surfaces with varying crystallinity. Five materials were modelled including nanocrystalline (NC) and polycrystalline (PC) copper and carbon as well as amorphous carbon (aC), and simulated to assess the effect of grain boundary, crystallinity, and chemistry of the material on the charge transfer mechanisms at the BamABCDE protein–substrate interface within the bacterial outer membrane. The simulation outputs were assessed using charge distribution, potential energy root mean square deviation (RMSD), radius of gyration (Rg), root mean square fluctuation (RMSF), backbone dihedrals, residue displacement, and Ramachandran plot. Copper based substrates, particularly NC Cu, showed faster kinetics of protein destabilisation (strongly bactericidal behaviour), marked by an increased torsional strain and loss of secondary structure. In contrast, carbon substrates, especially aC, preserved structural integrity and maintained stable electrostatic profiles, which suggested a bacteriostatic behaviour. What MD uniquely revealed at the atomic scale was a divergence in attack strategy between copper substrates: NC-Cu induced early and spatially focused backbone collapse through torsional perturbation, while PC-Cu caused widespread residue-level destabilisation through grain-boundary-driven electrostatic disruption. These deformation patterns emerged within picoseconds of interface formation, a timescale and spatial resolution not accessible through experiment, enabling direct visualisation of early protein unfolding, residue-specific displacement, and domain-level instability. These findings provide a pathway to advance atomic-level mechanistic understanding, enabling the purposeful design of highly efficient antibacterial coatings for applications in healthcare, transportation, food and industrial settings.

Keywords: bacteria-matter interaction; bactericidal surfaces; md simulation

1. Introduction

Bacterial contamination remains a persistent challenge across healthcare, food processing and industrial environments [1]. Surface-associated pathogens contribute significantly to hospital-acquired infections, biofilm formation and cross-contamination in sterilised environments [2], placing substantial pressure on public health and safety. These concerns are further amplified by the global rise in antimicrobial resistance [3], which has diminished the efficacy of conventional antibacterial strategies, including antibiotics, disinfectants and sterilisation protocols [4]. Chemical treatments, while often effective, carry risks of toxicity, environmental accumulation and the emergence of resistant bacterial strains [5]. As such, there is growing interest in surface-based antibacterial strategies operating through inherent physicochemical properties rather than external agents [6].

Among these, antibacterial surfaces composed of bactericidal metals and carbon-based materials have shown significant promise [7, 8]. Copper, in particular, exhibits bactericidal activity through mechanisms such as ion release, reactive oxygen species (ROS) generation and direct electron transfer to bacterial membranes (Fig. 1) [9-11]. In contrast, carbon-based surfaces, though typically non-redox active, exert bacteriostatic effects through interfacial charge interactions and hydrogen bonding, which may interfere with bacterial adhesion and protein function [12-14]. Prior experimental studies have demonstrated the efficacy of such surfaces, yet the underlying atomic-scale interactions that lead to these outcomes remain poorly understood [15, 16]. Here, MD presents a robust methodology to capture atomistic-scale events during the initial stages of protein–substrate interactions – within picoseconds - a timescale extremely challenging to probe experimentally [17]. While much of the existing literature relies on viability assays, microscopy and ROS quantification to characterise bacterial inactivation [18-20], these methods lack the temporal and spatial resolution required to resolve early-stage molecular events such as protein destabilisation [21]. Furthermore, prior studies often overlook the role of substrate crystallinity and surface charge in modulating these interactions [22]. As a result, the mechanistic understanding of how surfaces perturb the incipient protein structure remains unclear [23].

To address this knowledge gap, this work employs MD simulations to systematically investigate how surface chemistry and crystallinity influence the structural and electrostatic behaviour of a Gram-negative bacterium, specifically the BamABCDE protein complex embedded in the bacterial outer membrane. Five distinct substrates were selected for comparison: nanocrystalline copper (NC-Cu), polycrystalline copper (PC-Cu), nanocrystalline carbon (NC-C), polycrystalline carbon (PC-C), and amorphous carbon (aC). These substrates capture relevant variations in composition and atomic order, enabling a controlled examination of interfacial effects.

The study focuses on identifying early molecular responses such as charge distribution, backbone deformation and secondary structure disruption, which may precede gross morphological changes observed in experimental assays. Key

observables include potential energy, charge profiles, root-mean-square deviation (RMSD) [24], root-mean-square fluctuation (RMSF) [25], radius of gyration (Rg), residue displacement, dihedral angle distortion and Ramachandran mapping [26]. Through these metrics, this work offers mechanistic insights into the stability and structural response of surface-bound proteins.

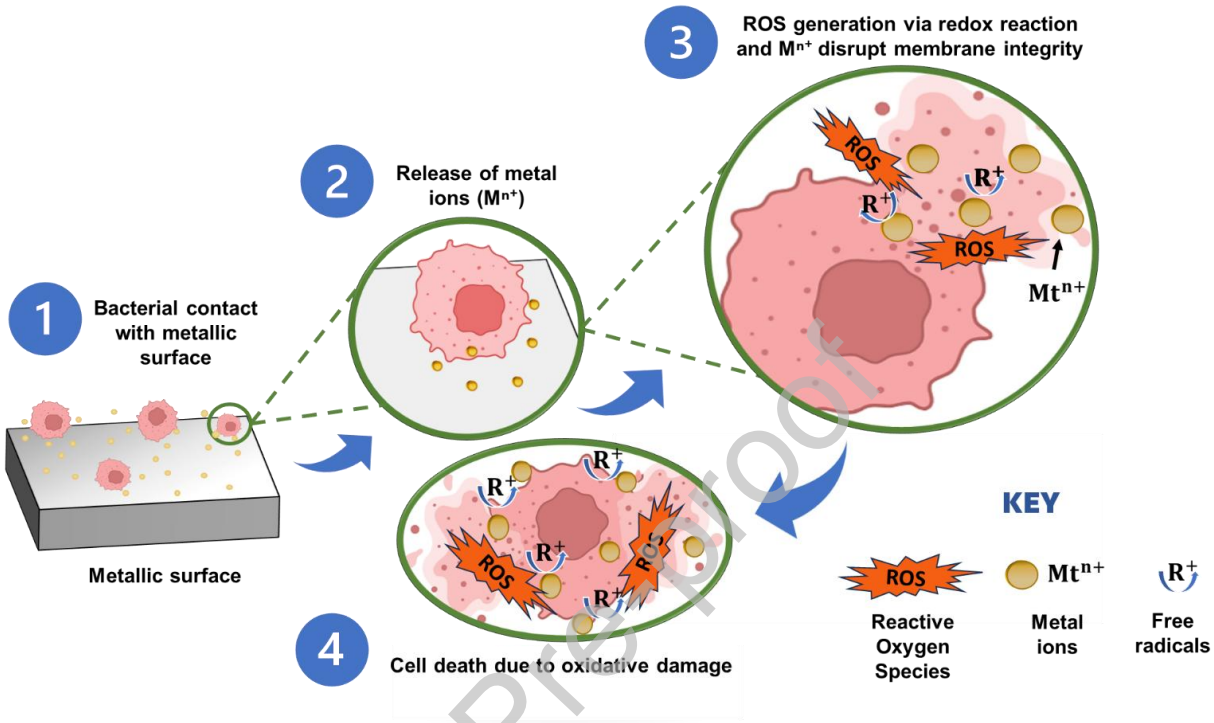

Fig. 1: Schematic illustration of metal ion-induced bacterial cell damage (author's own contribution). The interaction of metal ions with the bacterial membrane initiates a cascade of events, including the generation of ROS, lipid peroxidation, membrane disruption and ultimately leading to bacterial cell death.

The main research questions driving this study are:

- How do copper and carbon substrates, differing in crystallinity and composition, affect interaction with the protein structure through distinctive charge transfer mechanisms?
- Can early-stage molecular deformation of a bacterial outer membrane protein serve as a predictive indicator of the broader antibacterial efficacy observed at the colony level?
- What role does surface-induced charge distribution play in disrupting protein conformation?

By integrating atomic-scale MD simulations with structural (conformational stability, flexibility) and electrostatic (charge distribution, potential energy) analyses, this study determines how Cu and C substrates of varying crystallinity influence charge transfer and protein conformational changes in the bacterial outer membrane, supporting the design of antibacterial coatings.

2. Computational methods

2.1 Substrate model preparation

The work used few types of crystalline substrates with grain sizes of 5.35 nm and 5.45 nm for Cu and C, respectively, estimated from the average grain volume assuming spherical geometry, as well as aC containing about 40.8% of sp^3 bonds. The polycrystalline simulation models were generated by using an in-house developed Voronoi tessellation code with a total of twelve number of grains giving an individual average grain volume of about 79,261.1 Å³ for PC-Cu and 85,859.6 Å³ for PC-C, based on their respective simulation box dimensions [27].

aC was produced through a melt–quench process to yield structural disorder representative of amorphous phases following our previous work [28].

The Cu and C substrates were about 145.782 Å × 44.856 Å × 145.782 Å and 146.782 Å × 47.856 Å × 146.782 Å, respectively, ensuring comparable interaction areas between the protein and the substrates. The equilibrium lattice constants of copper and carbon for the REAXFF simulations were determined to be 3.738 Å (FCC) and 3.624 Å (diamond cubic), respectively.

2.2 Water-protein model preparation

The *Escherichia coli (E. coli)* BamABCDE protein complex with PDB ID: 5LJO [29] was selected as the representative model for this study due to its critical role in maintaining outer membrane integrity in Gram-negative bacteria. As a highly conserved β-barrel assembly machinery, it plays a central role in outer membrane protein folding and insertion, making it an ideal candidate for assessing structural responses to bactericidal surfaces.

The protein was solvated in a cubic periodic water box of size 145 × 145 × 145 Å using the TIP3P water model [30].The system was subjected to energy minimisation after solvation to remove steric clashes and to achieve a stable conformation. The minimised structure was subsequently equilibrated at 300 K using the same ReaxFF parameter set as that employed by Monti et al. [31], implemented in the LAMMPS simulation package [32]. After ReaxFF energy minimisation, the total system charge was confirmed to be zero; no counterions were added to avoid ionic screening effects and to isolate intrinsic protein–substrate electrostatics. To achieve a good equilibrium state, the modelled box containing water and bacterial protein was first equilibrated using an NPT ensemble for 500,000 steps using a timestep of 0.25 fs to permit the relaxation of volume and pressure fluctuations in the system under atmospheric pressure. This was followed by a further equilibration under the NVT ensemble for 500,000 steps to stabilise the system at constant temperature and volume. The sequential equilibration ensured thermodynamic stability before initiating

the substrate interaction. A visualisation of the fully solvated protein system, including surrounding water environment and initial configuration, is shown in Fig. 2.

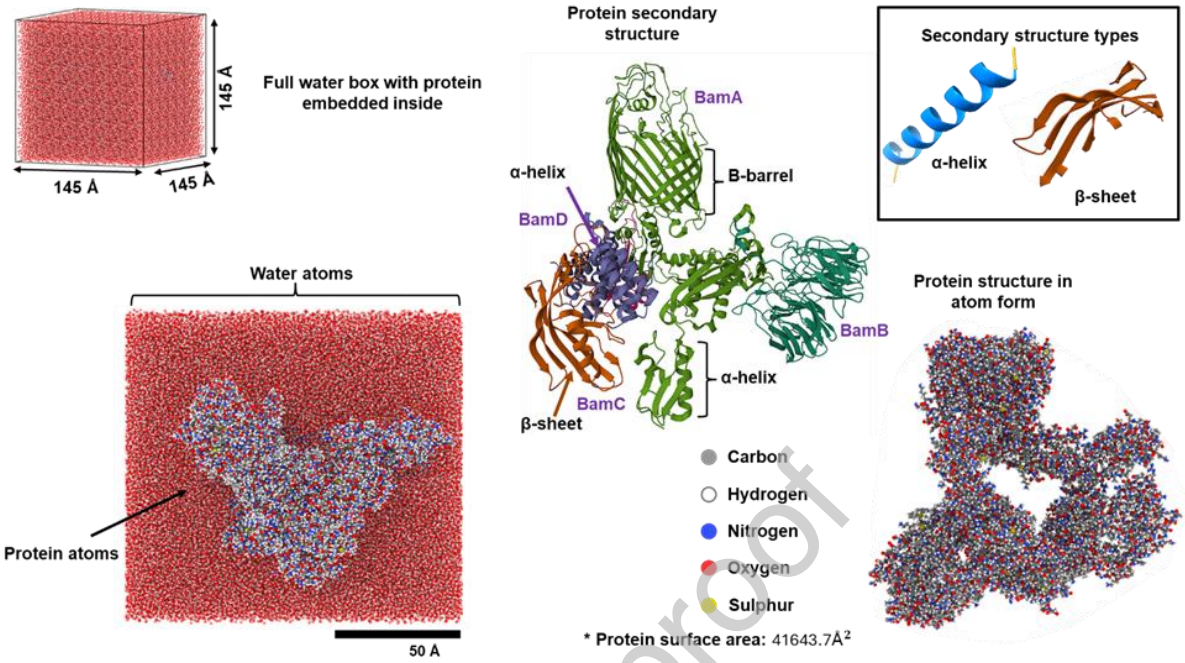

Fig. 2: All-atom representation of the BamABCDE solvated protein in a periodic water box model. The central panel shows the equilibrated protein within the water environment, while the surrounding view display orthogonal of the system configuration used for simulation and the protein secondary structure composition as well as protein structure in atom form. This setup was employed to ensure that the protein maintained its structural integrity and was fully immersed in the solvent environment prior to substrate interaction studies.

2.3 Water-substrate model preparation

A cubic water box measuring 145 × 145 × 145 Å was first generated via the CHARMM-GUI interface to serve as the solvent environment. This setup was consistent with the solvated system used in the protein–water preparation, allowing uniformity in simulation dimensions and boundary conditions.

Each five substrates were positioned beneath the water box to create the water–substrate interface. Prior to placement, a dimer energy analysis was performed to determine the optimum binding distances between key interfacial atom pairs (Cu–O, Cu–H, C–O, and C–H). This calculated distance between the substrate and water ensured the precision atomistic contact at the interface, as illustrated in Fig. 3a. As a result, copper substrates were positioned 3.7 Å below the water surface and carbon substrates 3.45 Å below, as illustrated in Fig. 3b.

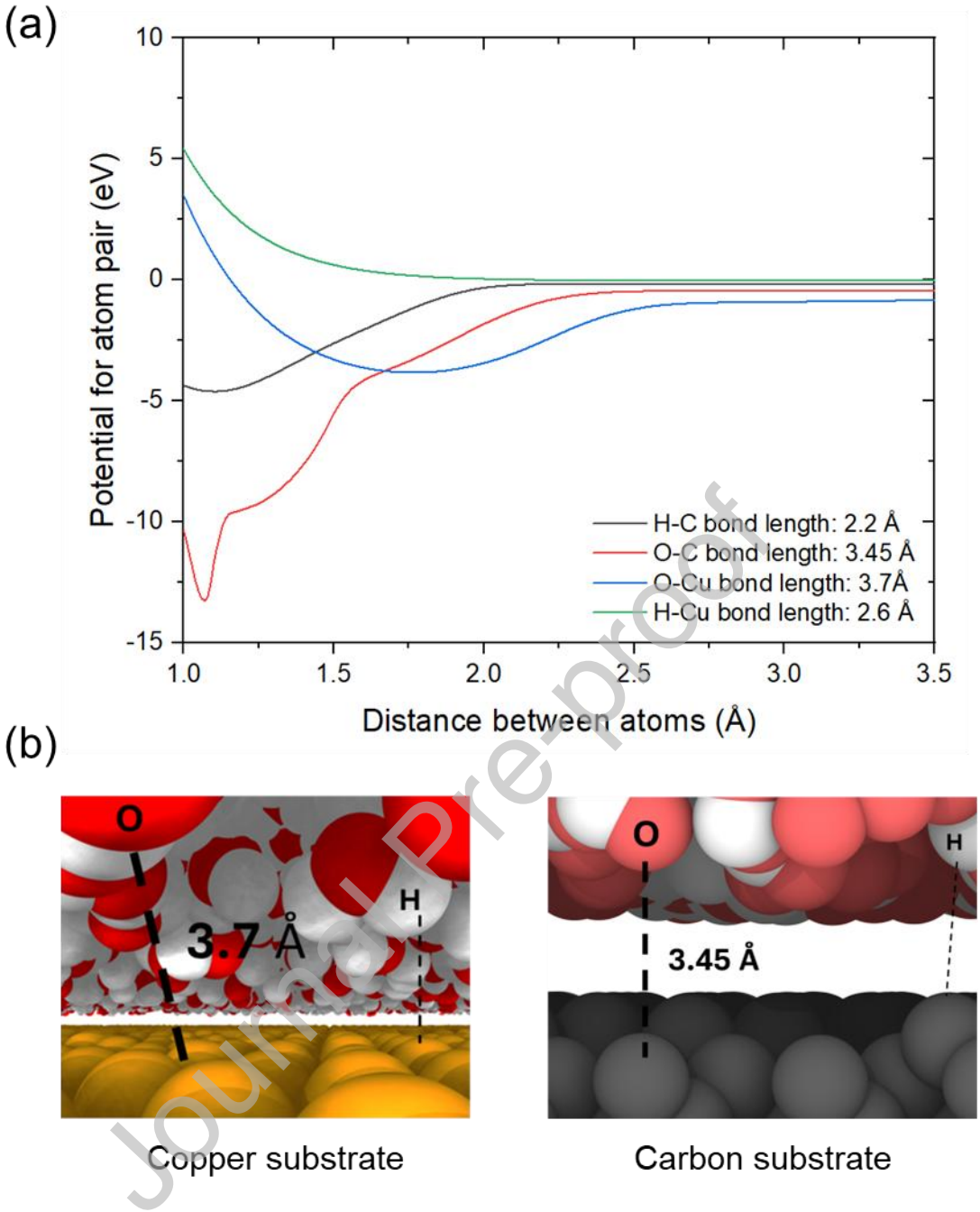

Fig. 3: (a) Dimer energy profiles for Cu–O, Cu–H, C–O and C–H atom pairs computed using ReaxFF and (b) atomistic illustrations of the interface between the water layer and NC-Cu and NC-C substrates.

Initial equilibration under the NPT ensemble was conducted for 50,000 steps with a 0.25 fs timestep to allow for pressure and volume relaxation. This was subsequently followed by an equilibration phase under the NVT ensemble for an additional 50,000 steps to maintain temperature stability. This two-phase equilibration ensured a stable thermodynamic baseline to investigate charge analysis in the following results and discussion section.

2.4 Protein-water-substrate assembly

Pre-simulation validation steps were performed to establish the electrostatic stability and physical accuracy. In this complex multi-material environment, it is important to ensure traceability and accuracy of the results in a stepwise manner. The work began with modelling a small water box to extract the baseline measurement charge of hydrogen and oxygen atoms. As shown in Fig 3a, the per-atom charges of oxygen and hydrogen were obtained as −0.8 e and +0.4 e, respectively, with a net charge of the system approaching zero. Following this exercise, a protein molecule was embedded into this box and the overlapping water molecules were removed. The charges on the water molecules were reextracted and these can be seen in Fig. 3b, both before and after the equilibration process. These two steps assertively gave confidence in no loss of information during the bacterial protein insertion into the water box. The next crucial step was the insertion of the substrate into this bacteria and water containing box and positioning the substrate at a right distance from the water surface to avoid molecular repulsion.

To perform this step, ReaxFF potential was used to calculate the dimer energy to determine the optimum binding distances for key interfacial atom pairs (Cu–O, Cu–H, C–O, and C–H) results shown in Fig. 3a).

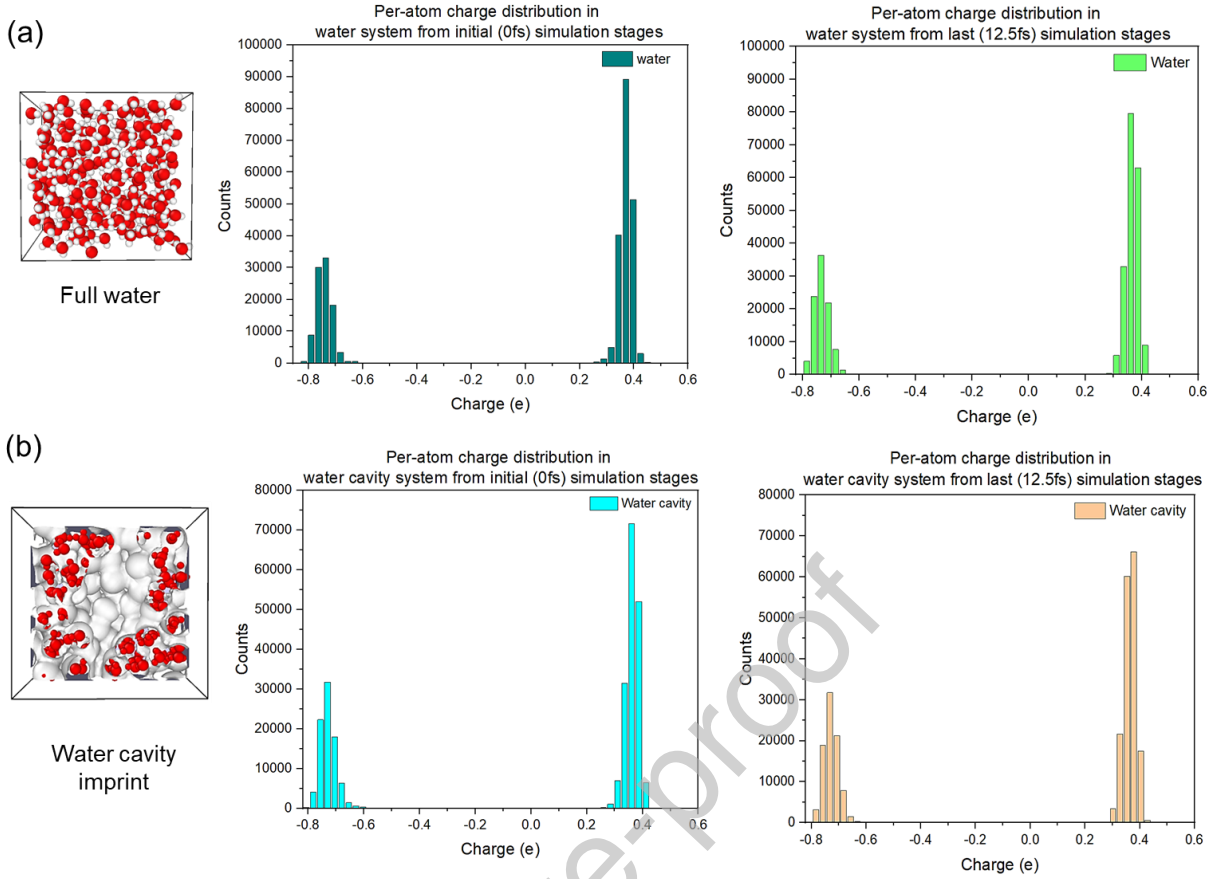

Fig. 4: Pre-simulation validation and interface optimisation. (a) Per-atom charge distributions in the full water box at the beginning and end of simulation confirm oxygen and hydrogen charges of −0.8 e and +0.4 e, respectively, with overall charge neutrality maintained. (b) Charge distribution in the modified water cavity after exclusion of overlapping water molecules, showing consistency across initial and final stages.

The final simulation box dimensions after the equilibration process were measured to be 145.782 Å × 193.506 Å × 145.782 Å for the copper-bacteria-water system and 146.782 Å × 196.256 Å × 146.782 Å for the carbon-bacteria-water system respectively. These crucial steps to prepare the MD model system ensured sufficient water padding above the protein, preventing artefacts from periodic boundary conditions.

The combined environments were equilibrated in the NVT ensemble at 300 K using ReaxFF with a 0.25 timestep. Each system was simulated for 1 million steps to capture the dynamic interactions at the protein-substrate interface. The NVT ensemble was chosen to keep the volume constant due to the fixed surface dimensions, so that the structural rearrangements and interactions would take place at controlled interfacial conditions.

2.4 Post-processing tools

Post-simulation analysis was carried out to characterise the electrostatic environment and structure dynamics of the solvated protein in contact with the modelled substrates. These included charge distribution, potential energy profiles, per-atom interaction forces, and conformational stability using root-mean-square deviation (RMSD), root-mean-square fluctuation (RMSF), and radius of gyration (Rg). Additional spatial and

temporal insights were obtained through cumulative residue displacement tracking and backbone dihedral angle (φ and ψ) analysis, along with Ramachandran mapping to examine conformational viability.

2.4.1 Charge distribution

Charge and energy data were extracted using custom LAMMPS scripts, while structural metrics and visualisations were processed using VMD and in-house Tcl routines.

2.4.2 Principal component analysis

Principal component analysis (PCA) was performed to evaluate substrate structural changes during the protein–surface interaction. PCA was applied exclusively to the atomic coordinates of each substrate extracted from the solvated MD trajectories. Three representative frames (0 ps, 125 ps and 250 ps) were used for each system to capture the initial, intermediate and final structural configurations. Prior to analysis, all frames were aligned to the initial substrate structure using a least-squares fitting procedure to remove global translational motion.

For each substrate, the Cartesian coordinates of all atoms were assembled into a data matrix, from which the covariance matrix was computed after mean-centering. Diagonalisation of the covariance matrix yielded eigenvalues and eigenvectors corresponding to the principal components (PCs). The first two components (PC1 and PC2), which describe the largest sources of structural variation, were retained for comparison across temperatures and substrate types. PCA projections were subsequently used to assess the extent of thermally induced atomic rearrangements, where clustering of points indicates minimal structural deviation and broader separation reflects modest relaxation of the substrate structure. All PCA calculations were performed using the MDAnalysis package.

2.4.3 Potential energy

Additionally, the potential energy of the protein was continuously assessed along the trajectories to determine its stability across different substrate interactions. Time-resolved total potential energy data were obtained from the LAMMPS outputs for comparison of energy trends that are associated with charge rearrangement or conformational transitions.

2.4.4 Root-mean-square-deviation

In order to quantify the differences in conformation of the protein structure during the simulation, the root-mean-square-deviation (RMSD) was determined from the Cartesian coordinate vectors r_i of all selected (typically backbone) atoms by comparing their positions at each trajectory frame to a reference structure, as illustrated in Equation (1):

$$RMSD = \sqrt{\frac{1}{N}\sum_{i=1}^{N}(r_i(t) - r_i^{ref})^2} \quad (1)$$

where $r_i(t)$ is the position of atom i along the trajectory at time t, r_i^{ref} is the position of atom i for the reference structure (initial), N is the number of atoms whose positions are being compared. RMSD calculations were preceded by least-squares fitting to remove global translation and rotation.

2.4.5 Arrhenius evaluation

Arrhenius evaluation was performed to assess the temperature dependence of structural deviation rates for NC-Cu and NC-C. For each temperature (100 K, 200 K and 300 K), an effective rate constant, k, was obtained from the time evolution of the RMSD by determining the characteristic time at which measurable conformational change first occurred. These rate constants were used to examine how quickly each system responded to thermal fluctuations.

The natural logarithm of the rate constant, $\ln(k)$, was plotted against the inverse temperature, $1/T$, to construct Arrhenius relationships for both substrates. Linear regression of the resulting plots provided the slope and intercept of the Arrhenius equation, allowing comparison of the apparent activation energies associated with early-stage structural deviation.

2.4.1 Radius of gyration

The radius of gyration (Rg) was computed to assess the overall compactness of the protein structure. It was determined as:

$$r_g = \sqrt{\frac{1}{N}\sum_{i=1}^{N}(r_i - r_{cm})^2} \quad (3)$$

where r_i is the position of atom, r_{cm} is the centre of mass of the protein and N is the number of atoms. A decrease in r_g suggests compaction and an increase in r_g indicated unfolding or structural relaxation.

2.4.2 Root-mean-square-fluctuation

The root-mean-square fluctuation (RMSF) was calculated to evaluate the local flexibility of each residue throughout the duration of the simulation. RMSF represents the time-averaged displacement of each atom from its own mean position, and was calculated using the expression shown in Equation (2):

$$\rho_i = \sqrt{\langle (x_i - \langle x_i \rangle)^2 \rangle} \quad (2)$$

where x_i is the Cartesian coordinate of atom i and $\langle x_i \rangle$ is its time-averaged position along the trajectory. RMSF was computed for backbone atoms to capture substrate-induced conformational flexibility.

2.4.3 Cumulative residue displacement

Cumulative residue displacement, which evaluate the long-term structural drift at the residue level, was calculated using VMD's Tcl scripting interface and displacements were averaged throughout the simulation trajectory to produce a residue-wise displacement profile. This metric tracks the absolute positional shift of each residue's Cα atom relative to its initial reference position at the start of the simulation.

Unlike local fluctuation metrics, cumulative residue displacement quantifies persistent, directional movement rather than oscillations about a mean. This enables the identification of residues undergoing sustained, irreversible conformational changes commonly associated with unfolding, domain rearrangement or loss of native contacts.

2.4.4 Backbone dihedral angle analysis (φ/ψ angles)

To evaluate local conformational changes in the protein secondary structure, dihedral angles φ (phi) and ψ (psi) were calculated for each frame throughout the simulation. These angles describe the rotation between peptide planes in the protein backbone and are key indicators of structural stability in α-helices and β-sheets.

The phi (φ) angle was defined by the torsion between four consecutive atoms: C(i−1), N(i), Cα(i), and C(i), corresponding to rotation around the nitrogen–alpha carbon (N–Cα) bond. The psi (ψ) angle was defined using the atoms N(i), Cα(i), C(i), and N(i+1), corresponding to rotation around the alpha carbon–carbonyl carbon (Cα–C) bond.

2.4.5 Ramachandran plot analysis

Ramachandran analysis was conducted to evaluate the distribution of backbone dihedral angles φ (phi) and ψ (psi) throughout the simulation. These angles, which define the torsional rotation around the N–Cα and Cα–C bonds, respectively, were calculated for each residue to assess whether they remained within sterically allowed regions associated with canonical secondary structures such as α-helices and β-sheets.

Residues occupying disallowed regions were identified as potential sites of local conformational strain or unfolding. This analysis provides insight into the preservation or disruption of secondary structure elements under different substrate conditions. The plots were generated using the built-in Ramachandran tool in VMD.

These analyses were carried out across all five substrates to compare how substrate crystallinity and composition influence protein charge distribution, structural stability, and local flexibility. These aspects are presented in subsections 3.1–3.3, respectively.

2.5 Statistical methods

Two independent MD simulations were performed for each substrate system (NC–Cu and PC–Cu) at 300 K using identical parameters but different random seeds to ensure independent sampling. Time-dependent quantities (RMSD and Rg) were analysed frame-by-frame across the two trajectories.

For RMSD and Rg, the mean and standard deviation (SD) between replicates were computed at each time point. Shaded regions in the figures represent ±1 SD. The overall reproducibility between simulations was quantified by comparing the trajectory-averaged values of each replicate using:

$$Percentage\ difference = \left(\frac{|\mu_1 - \mu_2|}{(\mu_1 + \mu_2)/2}\right) \times 100$$

Where μ_1 and μ_2 are the time-averaged values of the two trajectories.

For RMSF, residue-wise fluctuations were computed for each simulation, and the SD between replicates was calculated per residue. The mean SD across all residues was used as a measure of global reproducibility.

No hypothesis testing was performed, as the purpose of the statistical analysis was to quantify simulation variability rather than test differences between systems. All analyses were carried out in Python (NumPy, pandas, Matplotlib).

3. Results and discussion

3.1 Interfacial charge distribution and substrate PCA

3.1.1 Water–substrate charge transfer (without protein)

Understanding charge distribution at the substrate–water interface is critical for interpreting subsequent protein–substrate interactions. For metal environments such as copper, contact with a polar solvent like water can induce charge transfer and surface polarisation, which are relevant to phenomena such as corrosion and redox-driven antibacterial activity [33, 34]. Therefore, a preliminary charge analysis was carried out to establish a baseline electrostatic profile before introducing the protein.

The simulated system consisted of five individual substrates, each bonded to a water box placed directly above their surfaces to closely resemble realistic interfacial conditions. Videos illustrating water–substrate interactions and the associated interfacial charge transfer processes have been provided through Supplementary Videos.

Fig. 5 shows the temporal evolution of net surface charge for each substrate, where large differences are apparent due to their chemistry and structural characteristics.

Both NC-Cu and PC-Cu, as copper substrates, showed rapid and substantial increases in surface charge, reaching saturation levels of nearly 0.18 C in less than 4

picoseconds. NC-Cu achieved charge saturation at a faster rate, indicating a more intense and instantaneous interaction due to a larger gradient-less reactive surface facilitating rapid electron distribution with adjacent water molecules.

In contrast, carbon substrates, NC-C and PC-C, showed slower and weaker charge accumulation, reaching a plateau of about 0.05 C. This moderate charge buildup reflects intermediate electronic coupling due to the lower intrinsic conductivity and polarizability of carbon relative to metallic copper. The fact that NC-C and PC-C responses were similar asserts that the crystallinity differences among carbon substrates have negligible role on surface charge dynamics compared to copper.

The aC substrate among all substrates showed the weakest interaction, with minimal and slower charge accumulation, consistently remaining close to neutral throughout the simulation duration. This minimal charge buildup is consistent with the intrinsically disordered nature and low polarizability of aC, hence reflecting its limited capacity for polarization or charge transfer when in contact with water. This was emotive of the anticorrosive behaviour of a-C in sharp contrast to the other four combinations.

These results indicate that copper substrates and especially NC-Cu exhibit stronger electronic interactions with water compared to the carbon-based environments examined here. The electrostatic representation establishes a baseline for understanding how the water environment behaves in proximity to each substrate,

which is relevant to assessing subsequent charge transfer events involving the solvated protein.

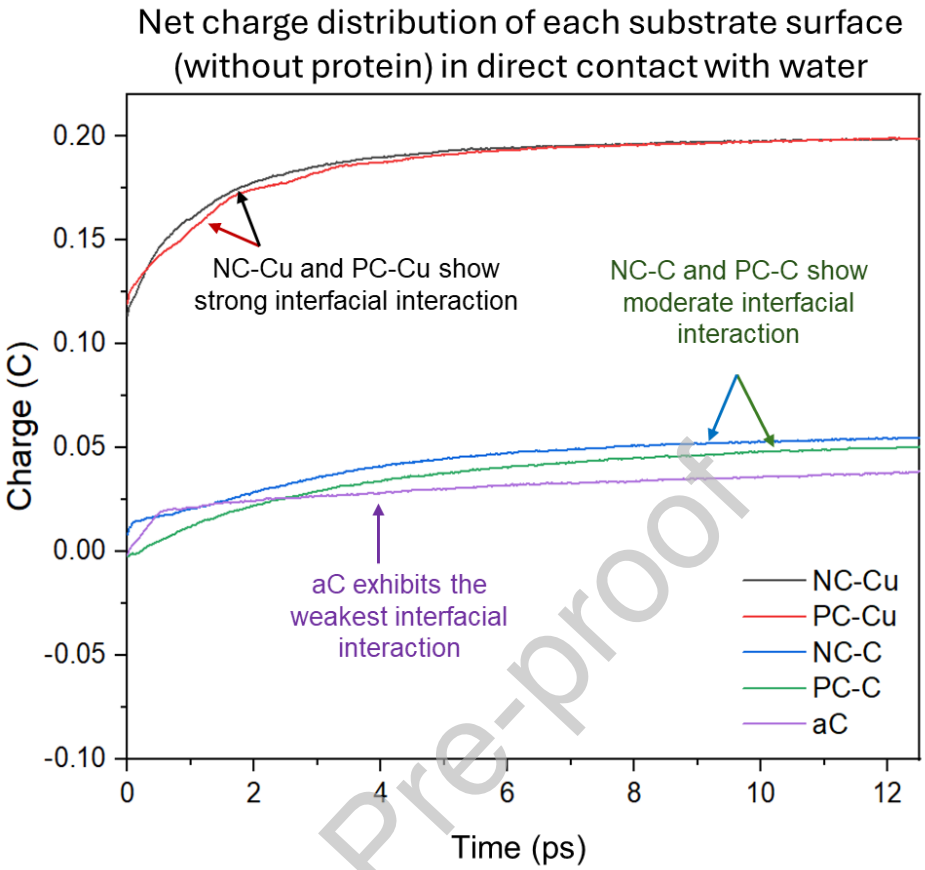

Fig. 5: Net charge distribution of each substrate surface (without protein) in direct contact with water during a 12 ps simulation. The plot represents electrostatic dynamics on the substrates (NC-Cu, PC-Cu, NC-C, PC-C, aC), highlighting charge transfer induced solely by substrate–water interactions.

3.1.2 Protein–water–substrate charge distribution

This section showcases the mechanics of charge transfer between various substrates and the water in the presence of a bacterial protein, which was later seen to denature.

After introducing the protein into the system, measurable changes in charge distribution were observed across all substrates, indicating substrate-dependent electrostatic responses. Fig 6(a,b) shows the simulation outputs in all five cases during protein-water-substrate interaction. The trend observed in the substrate was consistent with prior observations: NC-Cu and PC-Cu exhibited a rapid accumulation of charge, reaching a plateau at 0.2 C, whereas NC-C and PC-C showed a more gradual increase, approximately ~0.045 C. The aC substrate showed the least charge uptake. For completeness, the corresponding substrate-charge profiles at 100 K and 200 K for NC-Cu and NC-C are also included in Fig. 6(a). These lower-temperature simulations show only modest differences in the absolute charge levels and do not alter the substrate-dependent trends described above; therefore, the analysis presented here focuses on the 300 K results.

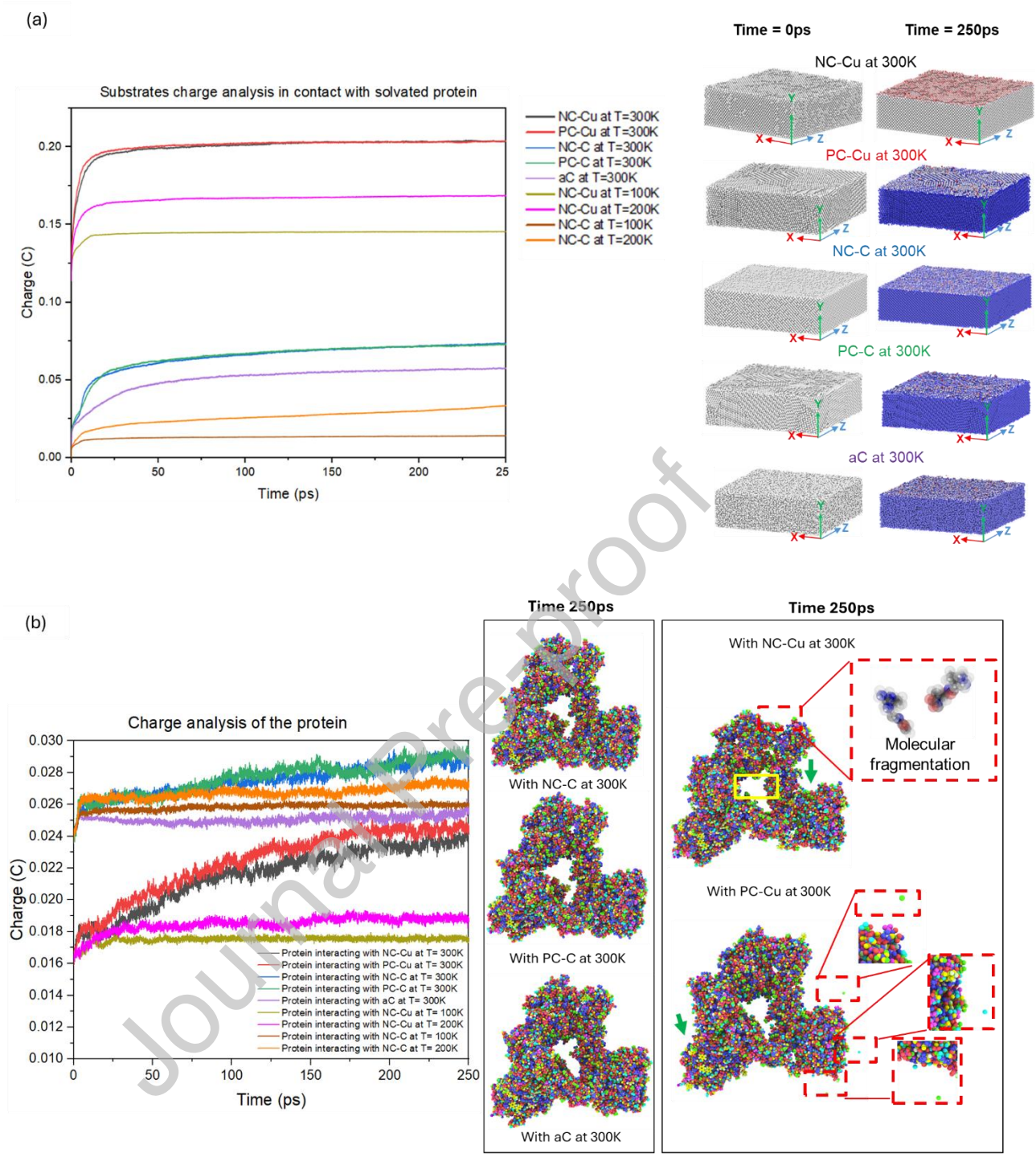

Fig. 6: Charge evolution in protein-water-substrate environments over 250 picoseconds: (a) net charge of each substrate in contact with solvated protein (with protein and water atoms removed for better visual aid) and (b) net charge of the solvated protein. Copper substrates both NC-Cu, PC-Cu show fast and substantial charge accumulation and polarisation, visualisation of protein charge effect for each substrate at temperature 300K is attached in the Supplementary Appendix A, showing places where structural unfolding occurred. Whereas carbon-based substrates, NC-C, PC-C and aC at temperature 300K show slower and lower charge transfer, no unfolding occurred in the protein structure even at the end of the simulation.

In addition, the protein showed large differences in its charge behaviour when dealing with different substrates. In NC-Cu and PC-Cu, the protein began with a lower net charge of approximately 0.016 C, which increased steadily to approximately 0.024 C. However, for NC-C, PC-C and aC, the protein initially was at approximately 0.024 C

and was experiencing minimal to moderate changes over time. This difference shows that the copper substrate has a stronger electrostatic influence on the protein right from the incipient stages. A visualisation of the protein unfolding is presented (see Supplementary Appendix A).

To test the stability of these electrostatic trends, the additional NC-Cu and NC-C simulations performed at 100 K and 200 K were also examined from the protein's perspective. For NC-Cu, the 200 K trajectory displayed the same initial rise in protein charge observed at 300 K, after which the charge fluctuated around 0.018 C rather than approaching a clear plateau. At 100 K, the protein similarly exhibited an initial increase during the first 10 ps, but began stabilising earlier, between roughly 15 and 17 ps, at a slightly lower level of charge approximately 0.017 C. For NC-C, both temperatures reproduced the characteristic early rise seen for NC-C and PC-C at 300 K; however, the subsequent behaviour differed. At 200 K, the protein charge did not follow a gradual increase but instead fluctuated between approximately 0.026 C and 0.027 C throughout the simulation. In contrast, at 100 K, the protein rose to around 0.025 C before maintaining a stable value for the remainder of the trajectory. Since atomic mobility is reduced at 100 K and 200 K, these simulations were included to demonstrate that the substrate-dependent charge behaviour identified at 300 K persists even under conditions where protein–substrate interactions are naturally diminished. This confirms that the charge evolution observed at 300 K reflects the intrinsic characteristics of the protein–substrate system rather than an artefact of running the simulation at a single temperature.

This difference is most likely the result of the higher polarization and electron affinity of copper, which can distribute the inner electron density of the protein upon contact. Although charge values that were extracted consider just the protein atoms, copper's strong electrostatic field polarises the local environment, indirectly influencing the protein's charge evolution. The carbon substrates, by contrast, generate relatively stable electrostatic environments, leading to less pronounced charge fluctuations.

Interestingly, while the final protein charge in copper environments (~0.024 C) mirrors the initial value observed in carbon environments, the underlying progression is fundamentally different. In copper environments, the protein begins with a lower net charge, which rises steadily over time. This increase coincides with the gradual loss of structural integrity, as secondary structural elements unfold and atomic order becomes destabilised. The elevated charge reflects intensified electrostatic coupling during active binding and structural disruption. Over time, as the protein becomes increasingly dissociated, the charge approaches a plateau, indicating a state where further structural interactions are minimal. In contrast, carbon environments maintain a near-constant protein charge throughout, reflecting minimal perturbation and sustained structural integrity.

These observations reinforce the role of substrate crystallinity and surface chemistry in regulating biomolecular charge dynamics in an aqueous environment with implications for interfacial stability and potential energy transitions upon adsorption.

3.1.3 PCA of substrate structural behaviour during protein-water interaction

Principal component analysis (PCA) was applied to the atomic coordinates of each substrate to assess whether any structural relaxation or deformation occurred during interaction with the solvated protein. As shown in Fig. 7, the analysis was performed using three representative frames (0 ps, 125 ps and 250 ps) from each trajectory and the resulting PC1–PC2 distributions capture the dominant collective motions of the substrate atoms.

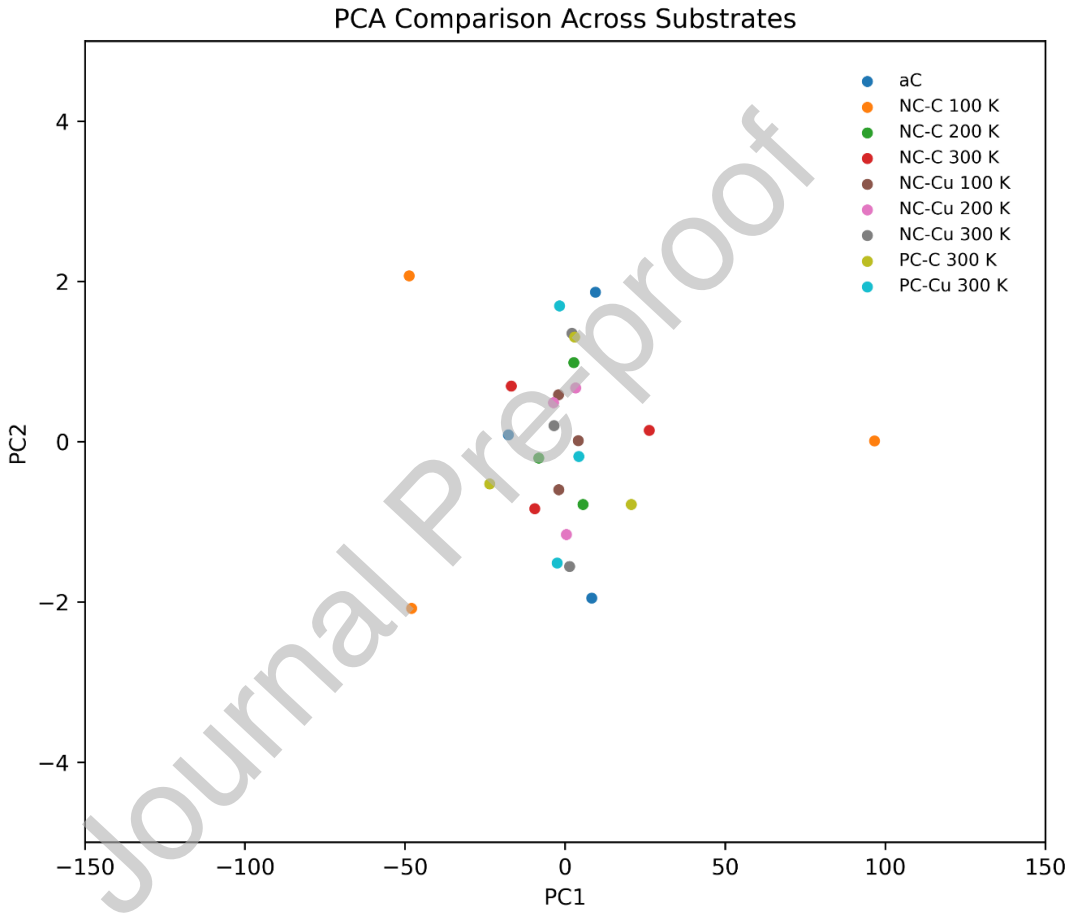

Fig. 7: PCA comparison of aC, NC-C, NC-Cu, PC-C and PC-Cu at 100, 200K and 300 K using three representative frames (0 ps, 125 ps, 250 ps). The tight clustering along PC1 and PC2 indicates only minor thermal relaxation, confirming that all substrates remain structurally stable during interaction with the solvated protein.

All substrates displayed compact PCA clustering, indicating that their underlying lattice structures remained stable throughout the simulation. For NC-Cu at 100 K and 200 K, the PCA points shift modestly along PC1 from negative to more positive values while PC2 remains within ±2, reflecting small thermal relaxation rather than structural change. At 300 K, NC-Cu forms a tighter cluster centred near PC1 approximately 0 with PC2 confined to ±1.5, demonstrating improved stability at that temperature.

NC-C exhibits similar behaviour, the 300 K trajectory shows a tight grouping near the origin, whereas the 100 K and 200 K datasets display only minor PC1 shifts, again consistent with limited relaxation rather than deformation. PC-C and PC-Cu produce the most compact clusters of the crystalline systems, reinforcing their structural rigidity and minimal thermal drift. aC also shows a small overall spread, which is consistent with its structurally disordered nature and limited capacity for coordinated atomic rearrangements. The tight clustering of PCA points indicates that aC remains highly stable throughout the 250 ps.

Overall, the PCA results show that all substrates retain structural integrity across temperatures, with only minor thermal relaxation observed, confirming that any protein conformational changes originate from interfacial electrostatics rather than substrate deformation.

3.2 Protein structural stability and conformational changes

3.2.1 Protein's potential energy

In this work, the protein's potential energy refers specifically to its bonded intramolecular energy, comprising contributions from bond stretching, angle bending, dihedral rotation and improper terms. This quantity reflects the stability of the protein's internal structure and does not include non-bonded interactions such as van der Waals or Coulomb forces with the surrounding solvent or substrate. Accordingly, variations in bonded potential energy are interpreted as changes in the protein's internal conformation.

The potential energy profiles for the interaction of the solvated protein with the various substrates are shown in Fig. 8. In all cases, the bonded potential energy begins with comparable values of approximately –1.222 eV. However, as the simulation progresses, the potential energy diverges between systems, indicating distinct substrate-dependent effects on the protein's structural stability.

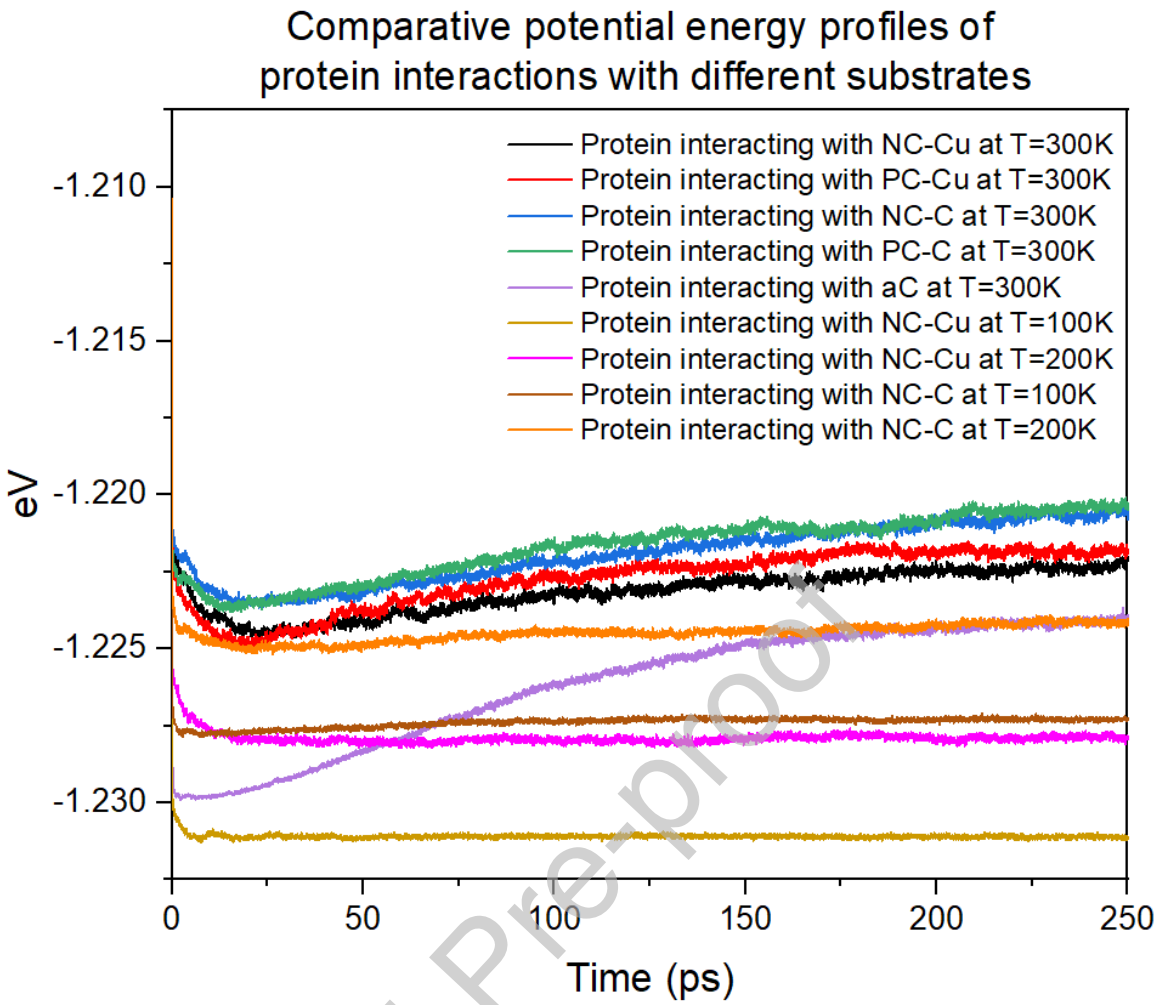

Fig. 8: Comparative potential energy profiles of the solvated protein interacting with different substrates over 250 ps. At 300 K, NC-Cu and PC-Cu show a rapid early decrease in potential energy followed by a plateau, consistent with significant structural destabilisation. In contrast, NC-C and PC-C at 300 K maintain higher and more stable energy levels, indicating only minor perturbation of the protein structure, while the aC system shows the least variation over time. The corresponding simulations for NC-Cu and NC-C at 100 K and 200 K are also included; these display smaller overall energy changes, reflecting the reduced level of structural motion at lower temperatures, but do not alter the relative distinction between copper and carbon environments.

The NC-Cu and PC-Cu environments both exhibited a steep drop in the potential energy of bacterial protein within the initial 20 ps, followed by a plateau between 80 and 100 ps. This energy loss suggests intense atomic interactions among the protein-copper atoms leading to destabilisation of the structure of the protein. That is, the protein begins to lose its native conformation and its features such as beta-sheets become disrupted. Visual inspection of simulation trajectory (see Supplementary Appendix A) indicates that this stage is marked by unfolding of the protein backbone and displacement of individual residues from their original positions. The plateau phase corresponds to a partially unfolded state, where the protein is unable to retain its native compact structure and exhibits increased atomic fluctuations.

PC-Cu shows more substantial energy decline and sustained fluctuations for longer than 50 ps, likely due to increased reactivity at grain boundaries and the high degree

of chemical heterogeneity of the polycrystalline surface, both of which enhance protein–surface interactions.

Contrary to this, carbon-based environments, such as NC-C, PC-C and aC, do not exhibit any significant decrease in energy. Rather, the potential energy of the protein upon interaction with these surfaces remains relatively stable with a slight increase over the 250 ps simulation time. This suggests that the protein remains in its native conformation, with minimal or no perturbation in its global folding structure. The lack of any significant energy decrease indicates that the protein-carbon surface interaction is weak and insufficient to destabilise the protein or induce significant conformational changes. Among the carbon substrates, aC shows the least fluctuation, thereby attesting to its minimal effect on the protein's structural integrity. This stability is due to the chemical inertness and low polarizability of carbon substates, which restrict extensive protein–substrate interactions and preserve protein's structural integrity.

In addition, the simulations performed at 100 K and 200 K for NC-Cu and NC-C are also shown in Fig. 8. Despite the lower atomic mobility at these temperatures, the relative distinction between copper and carbon environments remains evident, indicating that the pronounced early-time energy decrease in copper systems reflects an inherent feature of the protein–substrate interaction.

These results indicate that the lower potential energy plateau observed in copper environments reflects conformational destabilisation rather than thermodynamic stability. Conversely, the higher and more stable energy profiles in carbon environments are associated with structural preservation and weaker perturbation of the protein's native state.

In addition to the bonded potential energy described above, the protein's non-bonded pair interaction energy was also evaluated, and the resulting time-resolved profiles are provided in Supplementary Appendix F. Unlike the bonded potential energy, which reflects only intramolecular stabilisation arising from bond, angle, dihedral and improper terms, the non-bonded pair energy represents the total interaction energy acting on the protein, including van der Waals, Coulombic and bond-order–dependent contributions with the surrounding substrate and solvent. ReaxFF updates bond orders dynamically, these non-bonded and short-range chemical interactions are incorporated into a single aggregated pair-energy term rather than being decomposed into separate classical contributions. Examination of the pair-energy trends therefore provides a complementary indication of the strength and character of the protein–surface interactions. As shown in Supplementary Appendix F, both copper substrates generate strongly attractive interaction energies, with PC–Cu exhibiting a more pronounced and dynamically fluctuating interaction profile compared with NC–Cu, consistent with its higher surface reactivity and structurally heterogeneous grain-boundary features.

3.2.2 RMSD analysis of the bacterial protein

To compliment the potential energy results, RMSD analysis was performed to measure the structural deviations in the protein backbone as a function of time. Fig. 9 shows that environments containing copper substrates undergo significant structural deviation. Both NC-Cu and PC-Cu exhibited RMSD values over 2.5 Å, which signifies extensive disruption from the native protein structure. These elevated values reflect large-scale atomic rearrangements consistent with progressive unfolding. These findings align with previous studies suggesting that RMSD values typically between 1.5 and 2.5 Å for well-folded proteins, with values exceeding below and from 3 Å indicates significant conformational disruption [35-37].

PC-Cu showed the highest RMSD during the early simulation phase, likely due to grain boundary-induced heterogeneity, which increases the variability and strength of local protein–surface interactions. NC-Cu demonstrated a delayed but steady increase, ultimately plateauing near 3.5 Å, suggesting sustained and cumulative destabilisation facilitated by high surface reactivity and increased interfacial contact.

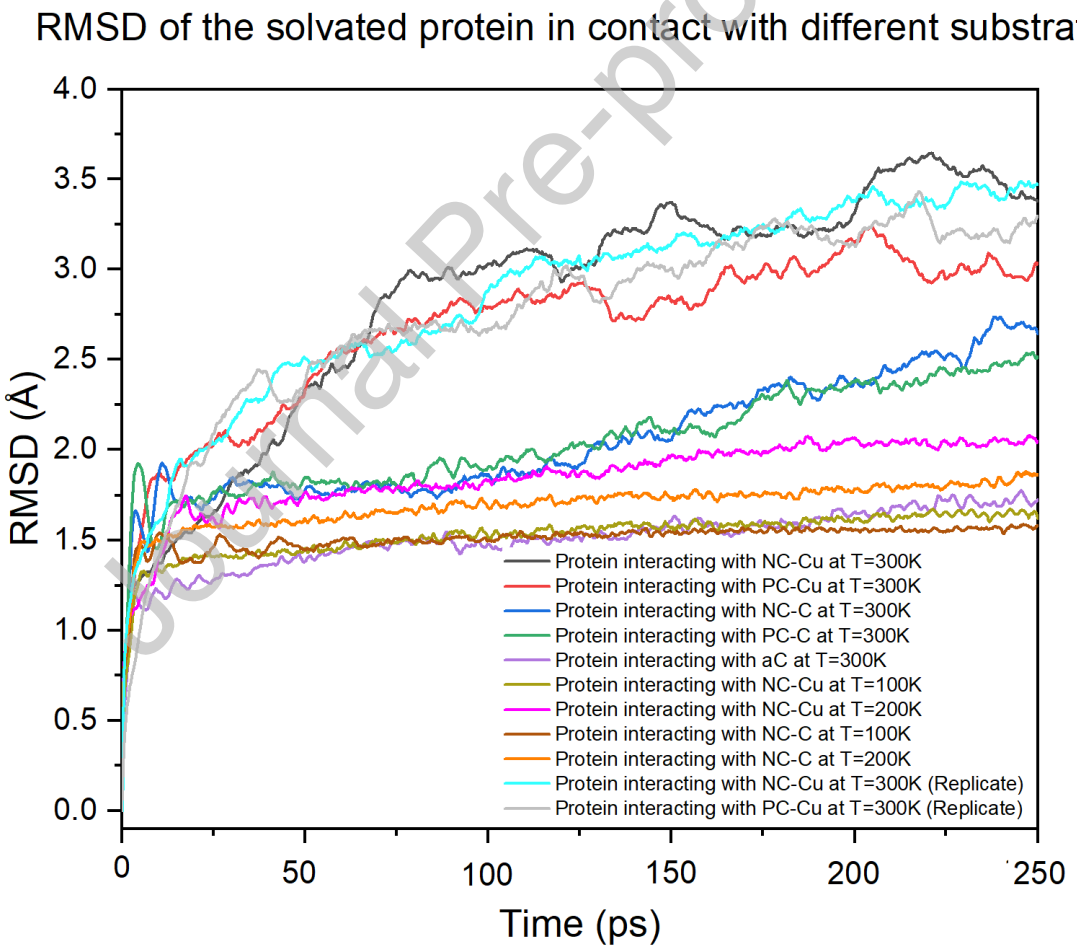

Fig. 9: Protein backbone RMSD over 250 picoseconds for each substrate system. At 300K, NC-Cu and PC-Cu show RMSD values exceeding 2.5 Å, indicating significant structural deviation and unfolding. NC-Cu increases steadily, plateauing at approximately 3.5 Å, while PC-Cu experience initial fluctuations. At 300K, NC-C, PC-C and aC exhibit more stable, lower profiles, with aC remaining at approximately 1.5 Å, consistent with preserved protein structure. The additional simulations for NC-Cu and NC-C at 100 K and 200 K are also shown; these display lower

RMSD amplitudes and earlier stabilisation, reflecting the limited structural movement at reduced temperatures without altering the relative ordering between copper and carbon environments.

For both NC-C and PC-C, RMSD values increased gradually from around 1.4–1.8 Å to around 2.25–2.5 Å, within the cutoff usually associated with partially folded or folded proteins. These moderate RMSD deviations indicate that the protein largely retains its tertiary structure, with only minimal conformational changes in response to the surface environment. The aC system yielding the lowest RMSD, stabilising at about 1.5 Å, indicative of an intact and compact protein structure. This stability is consistent with the minimal charge transfer and weak interaction observed for aC, limiting perturbation of the protein's architecture.

The simulations at 100 K and 200 K for NC-Cu and NC-C, also shown in Fig. 9, display small RMSD variations that remain well below the 2.5 Å threshold. For NC-Cu, the 200 K trajectory fluctuates modestly before settling approximately between 1.95 and 2.0 Å, while the 100 K trajectory converges near 1.5 Å after about 150 ps. For NC-C, the 200 K simulation approaches about 1.5 Å by 50 ps, and the 100 K simulation stabilises near approximately 1.4 Å following minor early-time fluctuations. These low-temperature profiles show limited overall deviation and simply reflect the limited structural conformation at these temperatures.

Additionally, to assess the reproducibility of the RMSD behaviour on copper substrates, an additional set of independent simulations was performed for NC–Cu and PC–Cu at 300 K using different random seeds. The replicate trajectories showed highly consistent RMSD profiles, with deviations remaining within narrow bounds throughout the simulation. SD bands and mean-RMSD traces for each system (see Supplementary Appendix E, Fig. S5) confirm that both NC–Cu and PC–Cu exhibit reproducible structural destabilisation, with replicate differences below 3% (see Supplementary Appendix E, Table. S1) across the trajectory. This statistical consistency demonstrates that the pronounced RMSD elevation on copper substrates is not an artefact of a single trajectory but instead reflects a robust, surface-driven destabilisation mechanism. In contrast, carbon-based systems, although not repeated, show RMSD magnitudes comparable to well-folded proteins and display no indication of variability that would challenge their observed stability.

RMSD analysis supports the previous assertion about the potential energy data by confirming that copper substrates cause substantial conformational destabilisation and the carbon-based substrates allow the protein to maintain structural integrity. These differences highlight the levels of interfacial effect that each type of substrates exerts.

3.2.3 Arrhenius analysis of structural dynamics derived from RMSD

Arrhenius analysis was performed to assess how the RMSD-derived rate constants change with temperature, using the structural deviation of the protein on NC-Cu and

NC-C as the defining event for comparison. Linear plots of ln(k) versus 1/T were generated to examine the temperature dependence of these rates.

As shown in Fig. 10, both substrates exhibit near-linear behaviour across 100 K, 200 K and 300 K, indicating that the early RMSD progression follows Arrhenius-type kinetics within this temperature range. NC-Cu displays a steeper slope than NC-C, reflecting a stronger temperature dependence during the onset of structural deviation, whereas NC-C shows a more gradual change in rate.

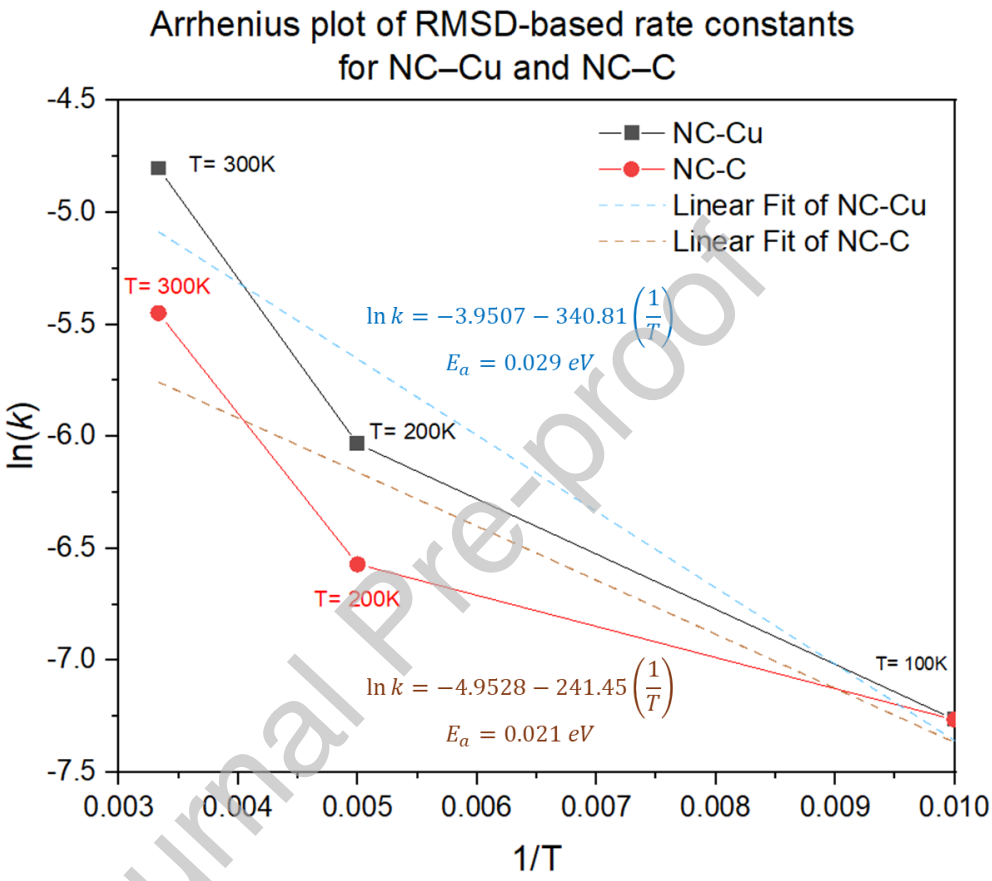

Fig. 10: Arrhenius plots of RMSD-derived rate constants for NC-Cu and NC-C at 100, 200 and 300 K. Both systems show linear ln(k)–1/T behaviour, indicating Arrhenius-type kinetics. NC-Cu exhibits stronger temperature dependence than NC-C, with apparent activation energies of 0.029 eV and 0.021 eV, respectively, reflecting early-stage conformational response.

The calculated activation energies are relatively small, approximately 0.029 eV for NC-Cu and 0.021 eV for NC-C, indicating early-stage conformational adjustments that occur before any large-scale structural rearrangement. These values therefore reflect the modest energetic barriers associated with the initial relaxation of the protein at the interface. Overall, the analysis shows subtle but measurable differences in how temperature influences the initial structural response of the protein when interacting with NC-Cu compared with NC-C.

3.2.4 Radius of gyration (Rg) analysis

The radius of gyration (Rg) was also analysed to determine the overall compactness of the protein structure. Rg measures the spatial distribution of atomic positions around

the protein's centre of mass, with lower values indicating a compact and folded structure and higher values reflecting structural expansion or unfolding.

Independent replicate simulations were also performed for NC–Cu and PC–Cu at 300 K using different random seeds. Both replicates produced closely matching Rg trajectories, with only minor fluctuations between runs (see Supplementary Appendix E, Fig. S6). The agreement between replicates demonstrates that the substrate-dependent changes in compactness are robust features of the system and not artefacts of a single trajectory.

The copper substrates, especially NC-Cu showed the highest increase in Rg, indicating reduced structural compactness and protein expansion undergoing reaction [38, 39], which increased steadily from about 44.0 Å to 44.7 Å, as shown in Fig. 11. This increase is concurrent with RMSD and potential energy values, reflecting substantial unfolding and structural destabilisation. Structural perturbation is a result of strong interfacial interactions in the form of electrostatic attraction, significant charge distribution and direct-atom-to-atom interactions between copper surface atoms and charged/polar protein residues. PC-Cu also showed the same trend, with Rg rising to around 44.2 Å. Polycrystalline copper surface, grain boundary and chemically heterogenous in nature, is the cause of variable interactions leading to structural perturbations.

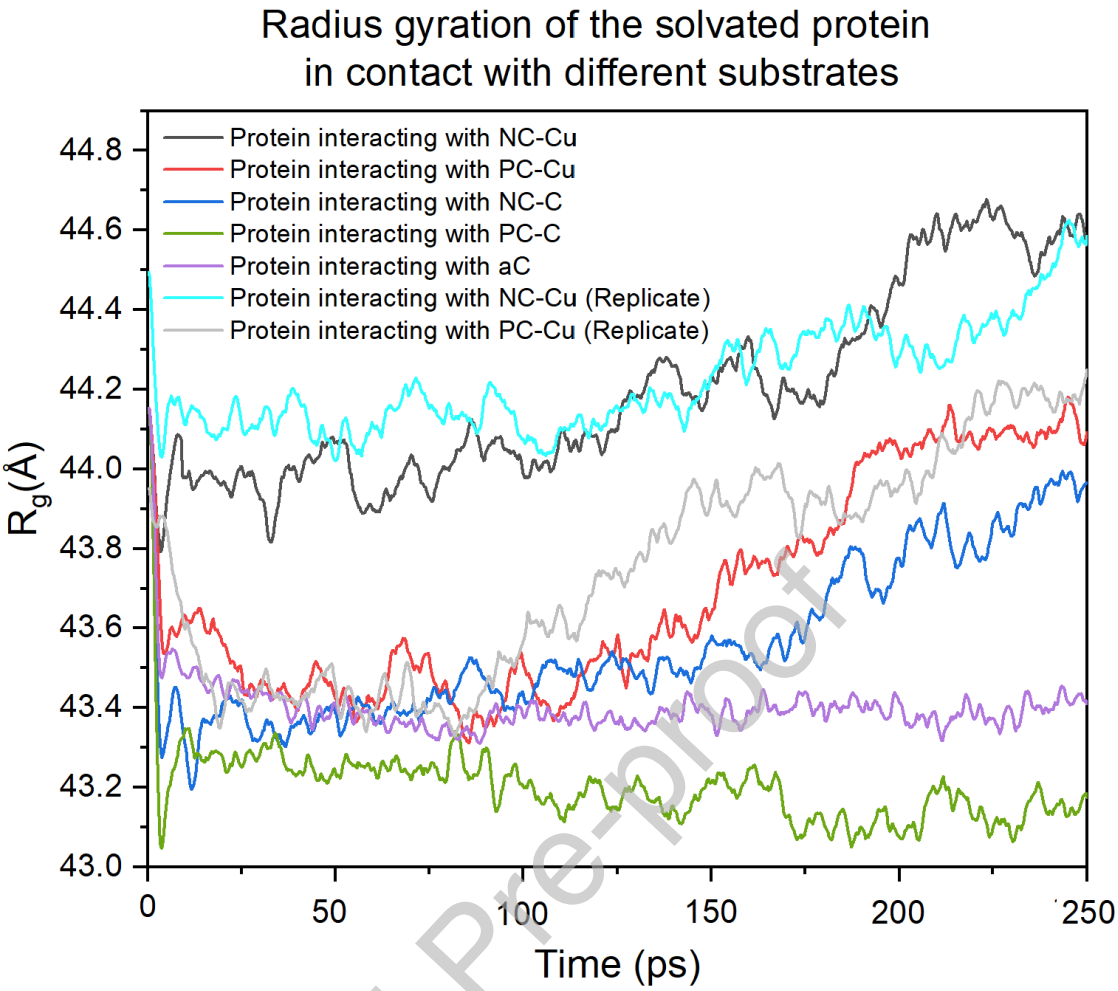

Fig. 11: Solvated protein Rg over a 250 picoseconds simulation, with variations in structural compactness in contact with different substrates. NC-Cu and PC-Cu exhibit steady increases in Rg, reaching approximately 44.7 Å and 44.2 Å respectively, denoting significant unfolding and structural destabilisation. Carbon substrates exhibit lower, more stable values, with PC-C and aC maintaining the lowest Rg, consistent with minimal structural disruption.

In contrast, carbon substrates showed a decreased and stable Rg values, PC-C maintained the lowest value at approximately 43.2 Å with very little change in structure. The aC system showed stable values at approximately 43.4 Å, demonstrating minimal interfacial interactions and negligible structural disruption. NC-C showed an increase but lower than copper-induced values. These findings confirm that copper substrates facilitate protein unfolding and carbon substrates maintain protein structure integrity.

Radius of gyration analysis clearly illustrates substrate-dependent protein compactness and structural stability change. Although global descriptor such as Rg and RMSD provide insights into overall conformational changes, these descriptors alone do not reveal residue-specific structural dynamics. To address this limitation and obtain further understanding of local protein flexibility, residue-level fluctuations were analysed using root-mean-square fluctuation (RMSF), as discussed in detail in the subsequent section.

3.3 Local flexibility and residue-level fluctuations

3.3.1 RMSF analysis

RMSF is used to assess residue-level flexibility along the protein backbone in various substrate environments. RMSF calculates a time-averaged measure of atomic positional deviation that allows the identifications of structurally labile regions and quantifying local fluctuations upon perturbation of the environment. This parameter is commonly used to infer local conformational flexibility and determine regions of unfolding or destabilisation at the residue level.

Independent replicate trajectories were generated for NC–Cu and PC–Cu at 300 K using different random seeds. Both replicates showed highly consistent residue-level fluctuation patterns, with minor (<9% difference between replicates) variation in peak intensities across the backbone (see Supplementary Appendix E, Fig. S7). The close correspondence between replicates confirms that the observed fluctuation profiles seen on copper substrates are reproducible characteristics of the system rather than artefacts of a single simulation.

As Fig. 12 shows, copper-based environments and more specifically PC-Cu, showed the highest residue-level fluctuations on the simulation. PC-Cu showed multiple peaks exceeding 6 Å, with isolated spikes reaching beyond 10 Å, which is illustrative of widespread localised destabilisation of certain secondary structural elements, thus reinforcing our arguments above. Fluctuations at such high levels (> 4–6 Å) typically indicate partial unfolding or structural disruption [40] events on β-sheets and α-helices and are reflective to strong electrostatic coupling and direct atomic interactions between the substrate and the structured domains of the protein.

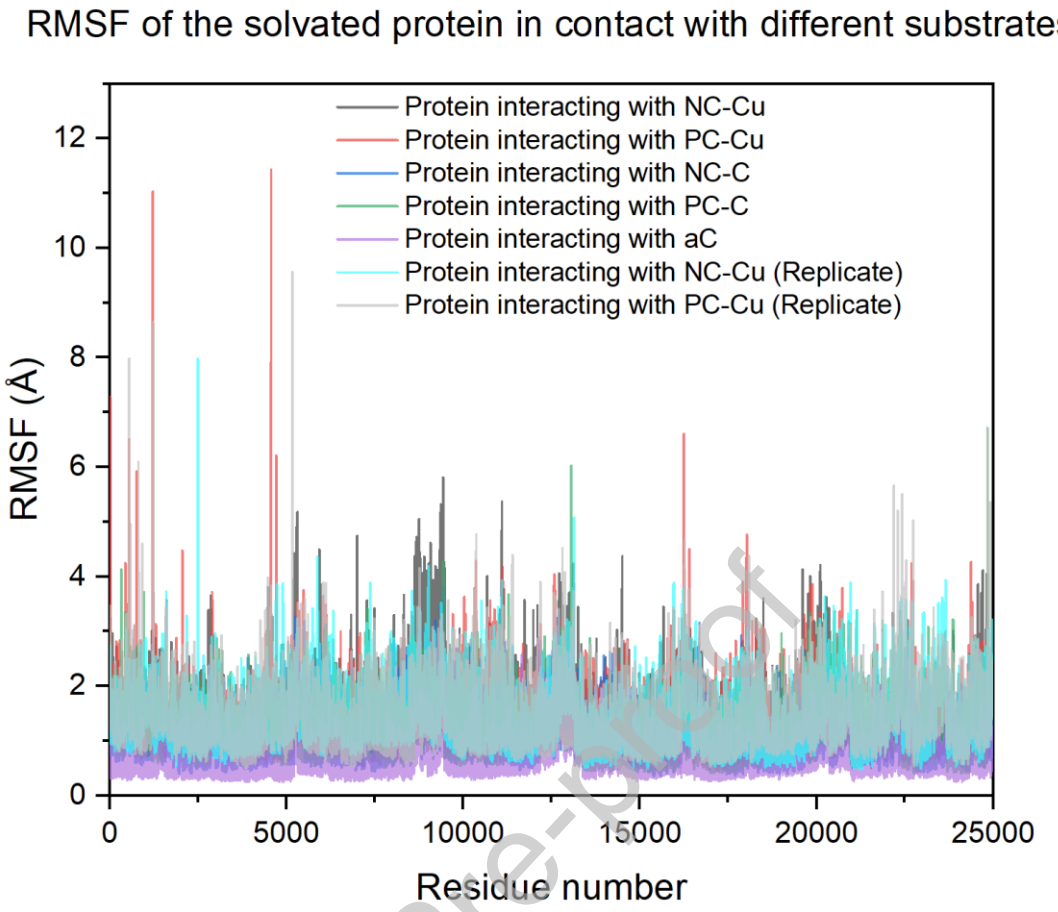

Fig. 12: Solvated protein RMSF profiles in contact with different substrates. NC-Cu and PC-Cu show higher RMSF values, with PC-Cu exhibiting peaks above 10 Å, which are signs of local destabilisation. NC-C, PC-C and aC have lower RMSF, which signifies greater structural stability.

NC-Cu also exhibited large fluctuations, with RMSF values of 4–6 Å consistently over long residue ranges. Sustained and high flexibility is reflective of broader conformational perturbation, consistent with global unfolding dynamics previously observed in RMSD and Rg analyses. The trend would indicate that NC-Cu, even in its nanocrystalline form, provides enough electrostatic and surface contact forces to compromise the stability of secondary structures.

By comparison, NC-C, PC-C and aC, exhibited significantly lower RMSF values. NC-C and PC-C maintained residue-level fluctuations in the range of 2–4 Å, indicating limited structural displacement and a relatively stable backbone conformation. The aC system generated the lowest fluctuations of all, rarely exceeding 2.5 Å, consistent with restricted atomic fluctuation and a compact, preserved fold.

Differential behaviour observed across environments supports the conclusion that copper substrates and more so PC-Cu, impose significant structural perturbations at the residue level, that destabilise α-helices and β-sheets. These fluctuations indicate compromised local structural cohesion and highlight regions prone to unfolding. In contrast, carbon substrates uphold local rigidity, suppressing residue-level fluctuation and maintaining secondary structure stability. To complement this analysis, the following section investigates cumulative residue displacement over time, providing

further insight into the regions that undergo long-term conformational drift beyond transient fluctuations.

3.3.2 Cumulative residue displacement

Cumulative residue displacement measures overall positional displacement of every residue from its origin structure throughout the simulation period. Whereas, RMSF indicates local fluctuations about a mean position, displacement identifies regions that undergo sustained, irreversible structural drift indicative of unfolding or disruption of native contacts. This measure distinguishes transient vibrations from persistent deviations, allowing for clearer identification of destabilised protein segments.

By mapping displacement patterns across residues, this analysis builds on RMSF results to show where regions progressively deviate from the native conformation upon substrate interactions.

As indicated by Fig. 13, patterns of displacement differed significantly with substrate type. Copper substrates induced the most significant conformational change. In the NC-Cu system, Fig. 13(a), residue-level displacement reached a maximum of 17.71 Å, mainly within the N-terminal domain. One highlighted region, residues 330 to 374, which correspond to the BamB subunit, contained loop and beta-sheet regions and showed gradual drift from as early as about trajectory frame 451, consistent with structural destabilisation. A second region, residues 100 to 107, mapped to BamC, the least stable subunit within BamABCDE after BamE. This region also showed significant displacement. BamC is an alpha-helical protein, however, lacks beta-sheet scaffolding, is partially disordered and contains solvent-exposed surfaces. Which its structure makes it prone and weak to surface perturbation.

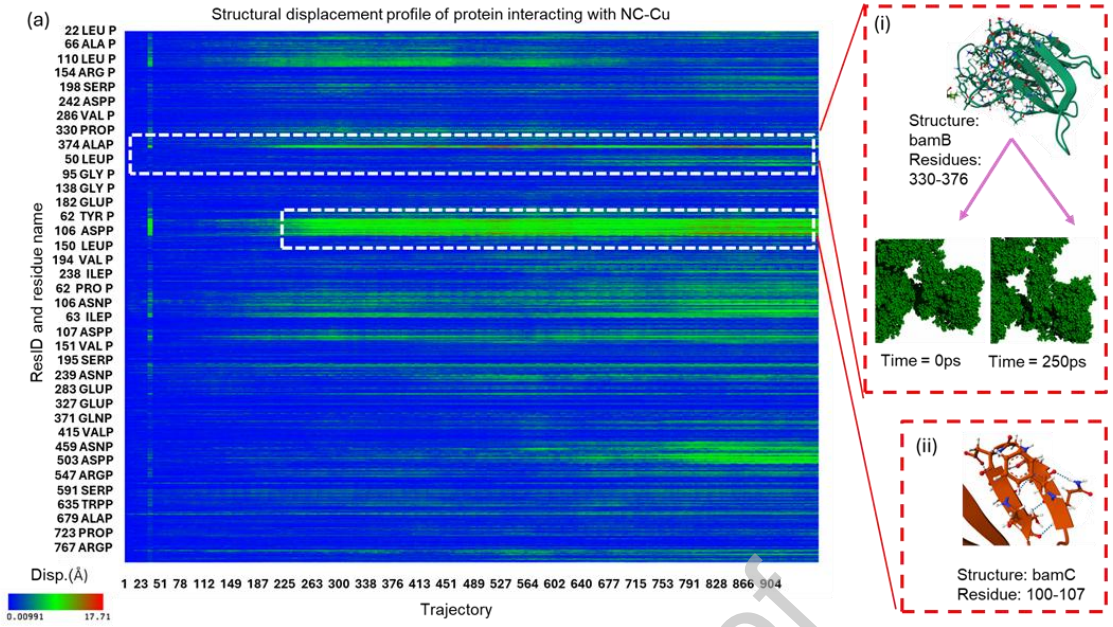

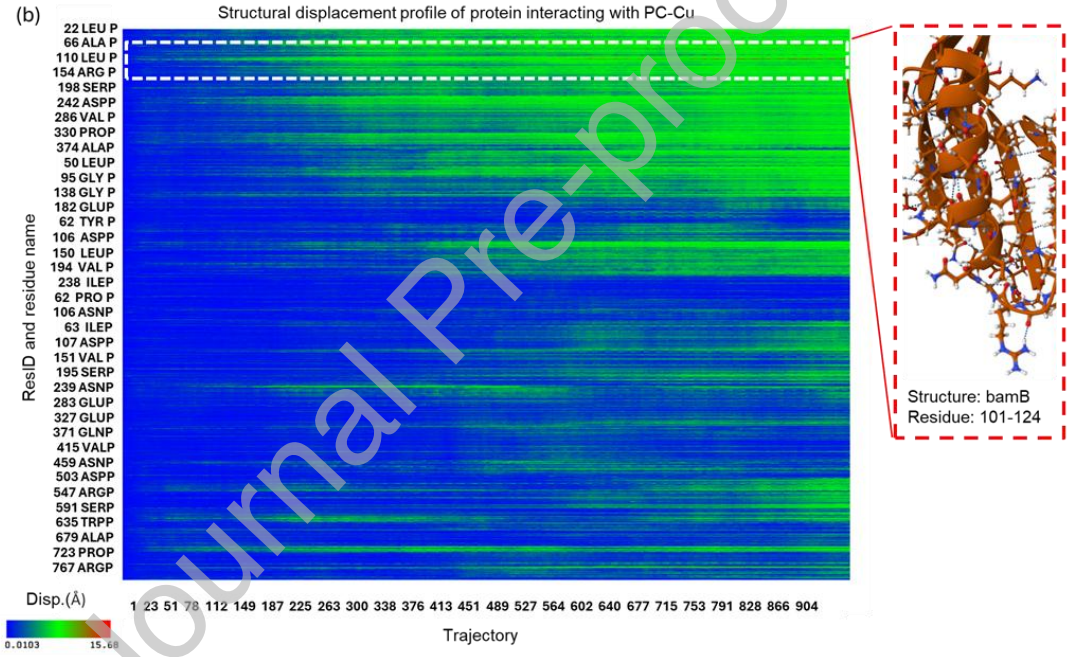

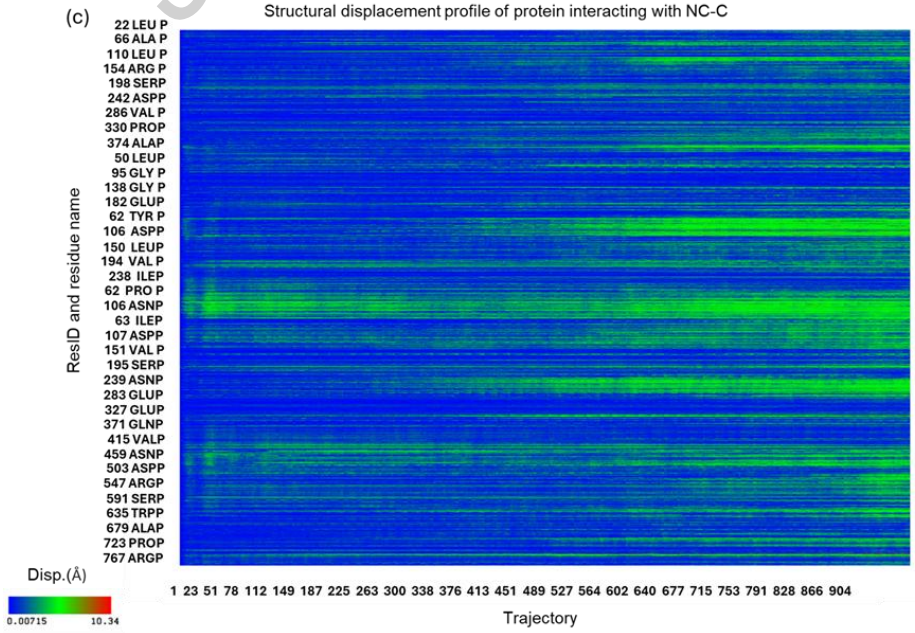

Fig. 13: Displays the cumulative residue displacement profiles for the bacterial BamABCDE protein across five substrate environments: (a) NC-Cu with inset (i) representing residues 330-376 of bamB showing their position in the protein at 0 picoseconds and 250 picoseconds, and inset (ii) shows bamC residues 100-107, (b) PC-Cu, (c) NC-C, (d) PC-C (provided in Supplementary Appendix B), and (e) aC (provided in Supplementary Appendix B). Regions of heightened displacement are highlighted in dashed boxes, representing substrate-specific conformational change. Significant structural deviations were observed in the BamB and BamC domains under copper-based substrates, whereas carbon-based environments exhibited lower displacement magnitudes, indicating structural integrity.

In the PC-Cu, Fig. 13(b), the maximum displacement of 15.68 Å in BamB was between residues 101 and 124. This segment contains an alpha-helix flanked by two short beta-strands linked by loops. Although the extent of deviation was lower than in NC-Cu, the displacement was localised in a structurally sensitive region, indicating partial unfolding and disruption of tertiary contacts.

Carbon substrates exhibited a divergent profile. NC-C, PC-C and aC all exhibited significantly lower displacement magnitudes, with no indication of disruption at the domain level. The aC system, as depicted in Fig 13(e) (provided in Supplementary Appendix B), showed the smallest overall displacement, with values remaining below 8.90 Å, exhibited twofold lower than those recorded for NC-Cu. NC-C and PC-C, Fig 13(c) and Fig. 13(d) (provided in Supplementary Appendix B), reached maximum values of 10.64 Å and 10.34 Å, respectively. These displacements were localised and did not extend throughout the entire structural domains. The displacement in these environments likely reflects minor loop flexibility or compacting rearrangements rather than unfolding.

Copper substrates therefore promoted irreversible residue migration and destabilisation in structurally labile regions, particularly in BamB and BamC. In contrast, carbon-based environments maintained spatial integrity and limited displacement, consistent with their increased conformational stability. This analysis complements the RMSF results by distinguishing transient fluctuations from permanent structural deviations and sets the foundation for evaluating whether these displacements correspond with alterations in backbone dihedral angles.

3.3.3 Backbone dihedral angle analysis (φ/ψ angles)

In proteins that are folded, φ and ψ angles typically fall within preferred regions. These appear as blue to green on φ/ψ maps, indicating conformational stability. Deviations into yellow, orange or red regions are indicative of increasing torsional strain, which is generally associated with local structural instability. While the present analysis uses colour mapping to visualise dihedral angle distributions, previous studies have similarly shown that alterations in φ and ψ torsion angles are closely tied to conformational changes in proteins. For example, Petrescu et al. [41] observed that during chemical denaturation, torsional shifts in φ and ψ angles toward β-strand regions of the Ramachandran plot accompanied the onset of structural destabilisation. Likewise, Palmisano et al. [42] employed atomistic MD simulations with metadynamics to map the energy landscapes of φ and ψ as collective variables, revealing that transitions in these angles drive the system toward intermediate states associated with unfolding. Additionally, other studies have also explored this structural change, further

supporting the notion that distortions in φ and ψ angles serve as early indicators of protein unfolding by marking regions of increasing conformational strain [43, 44].

In the NC-Cu system, Fig. 14(a), colour shifts from blue to green and red in the ψ angle plot indicate increased torsional variation. This suggests that the copper substrate perturbed the backbone conformation, particularly within residues 330–374 and 100–107. These deviations align with regions previously identified in the displacement analysis, supporting a link between ψ angle distortion and long-range structural reorganisation.

(a)

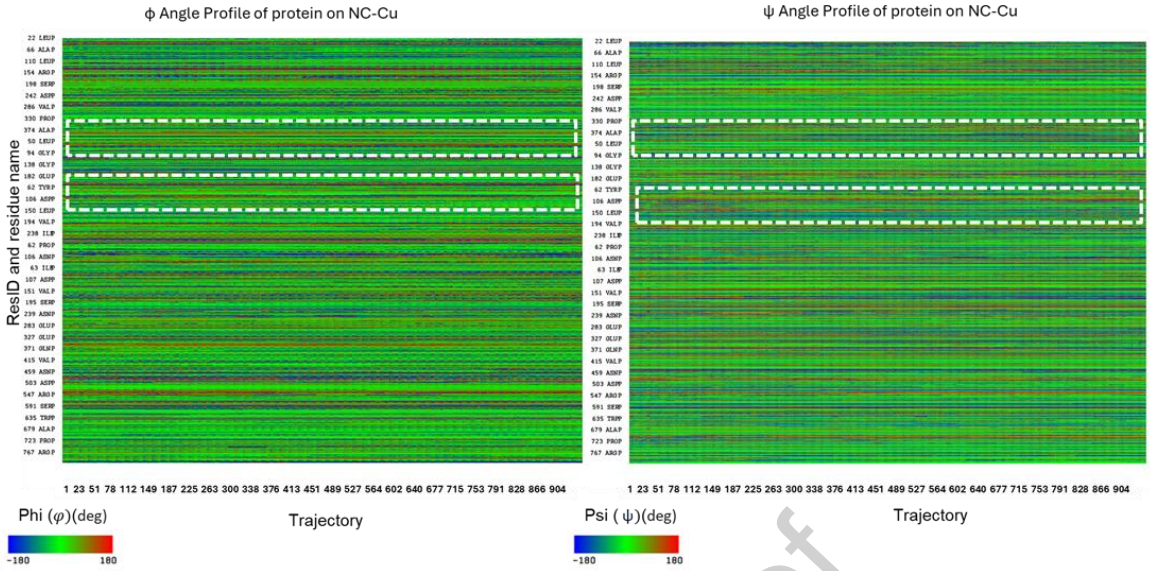

(b)

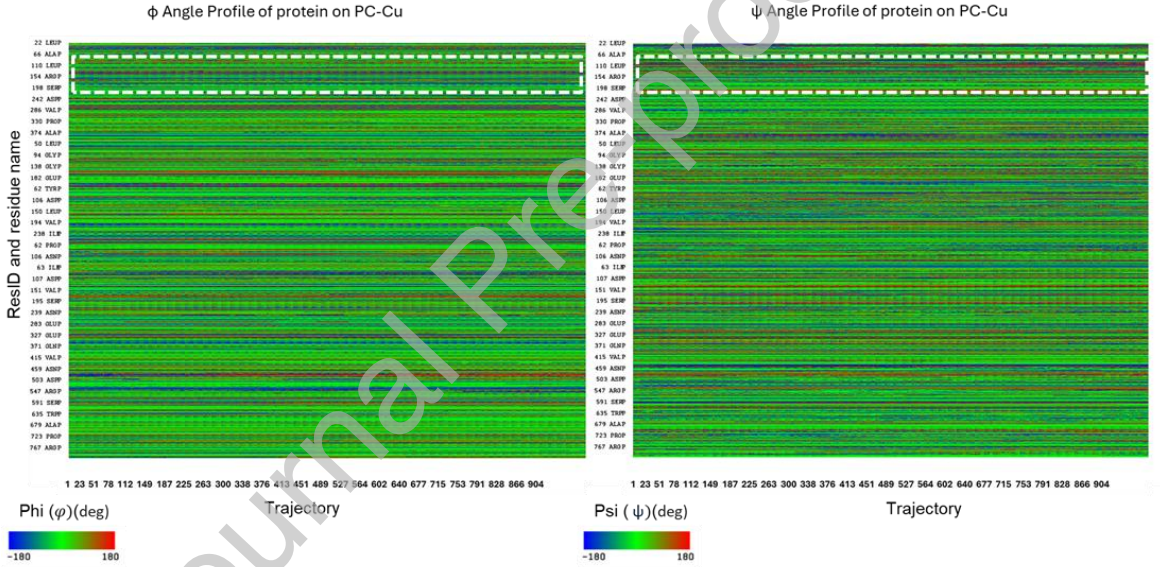

(c)

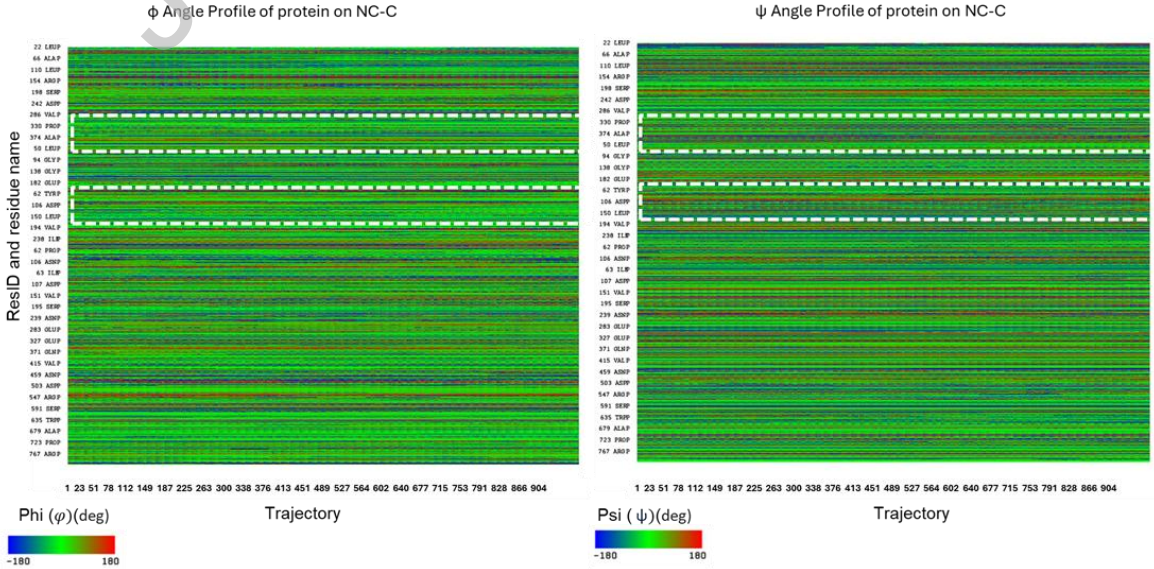

Fig. 14 Presents the distribution of the φ (left) and ψ (right) backbone dihedral angle of the protein across five substrate: (a) NC-Cu, (b) PC-Cu, (c) NC-C, (d) PC-C (provided in Supplementary Appendix C) and (e) aC (provided in Supplementary Appendix C). Each row in the figure represents an indivifual residue, and the x-axis represents simulation trajectory. The colour scale ranges from –180° shown in blue to +180° shown in red, with green indicating typical torsional states. Transitions to yellow or red reflect deviations from stable conformations. White dashed boxes mark regions previously identified with significant residue displacement. These profiles illustrate substrate-dependent torsional responses, with more pronounced angular shifts observed on copper-based surfaces.

The PC-Cu system shown in Fig 14(b), showed moderate ψ angle fluctuation while φ angles remained relatively stable. Regions of interest showed broader ψ angle changes without persistent red shifts. This trend suggests partial torsional disruption that may contribute to local instability but not extensive unfolding.

For the NC-C system, Fig. 14(c), φ and ψ plots remained predominantly green throughout the simulation. Residues 330–374 and 100–107 exhibited stable angular profiles, showing minimal torsional deviation. No sustained transitions into strained conformational space were observed. These observations are consistent with earlier displacement and RMSF analyses, showing structural stability on this carbon substrate.

The PC-C system, as shown in Fig. 14(d) (provided in Supplementary Appendix C), had a largely stable dihedral conformation. The φ angle plot showed occasional yellow fluctuations within residues 101–124, while the ψ plot showed a temporary blue to yellow colour transition with a later return to green in the trajectory. These transitions suggest minor angular adjustment without ongoing strain. Compared to PC-Cu, the PC-C substrate had a higher level of sustained torsional alignment.

For the aC system, φ and ψ dihedral angle plots, Fig. 14(e) (provided in Supplementary Appendix C), show even green distribution across the simulation, indicating that torsion angles remained in normal conformational limits. There is minimal colour variation observed, with no sustained deviation into red or yellow regions. This is indicative of a stable backbone conformation with a lack of torsional strain. The absence of large deviation in both φ and ψ indicates that the aC substrate maintained torsional integrity throughout the trajectory. These results are consistent with the previously observed low RMSF and displacement values, confirming that aC imposes minimal structural perturbation.

3.3.4 Ramachandran plot analysis

Ramachandran plots are widely used to evaluate protein structural quality, as they sensitively reflect backbone torsion angles for each residue [45-47]. Ideally, residues should occupy favoured regions corresponding to α-helices and β-sheets, while a higher occupancy in disallowed regions is indicative of poor structural integrity [48] and unfolding tendency.

As illustrated in Fig. 15(a) and 15(b), NC-Cu and PC-Cu environments had broader angle distributions extending into disallowed regions represented by light and dark blue. Such deviations represent torsional distortion and secondary structure

disruption, consistent with the high residue flexibility and spatial transitions observed in previous RMSF and displacement analyses.

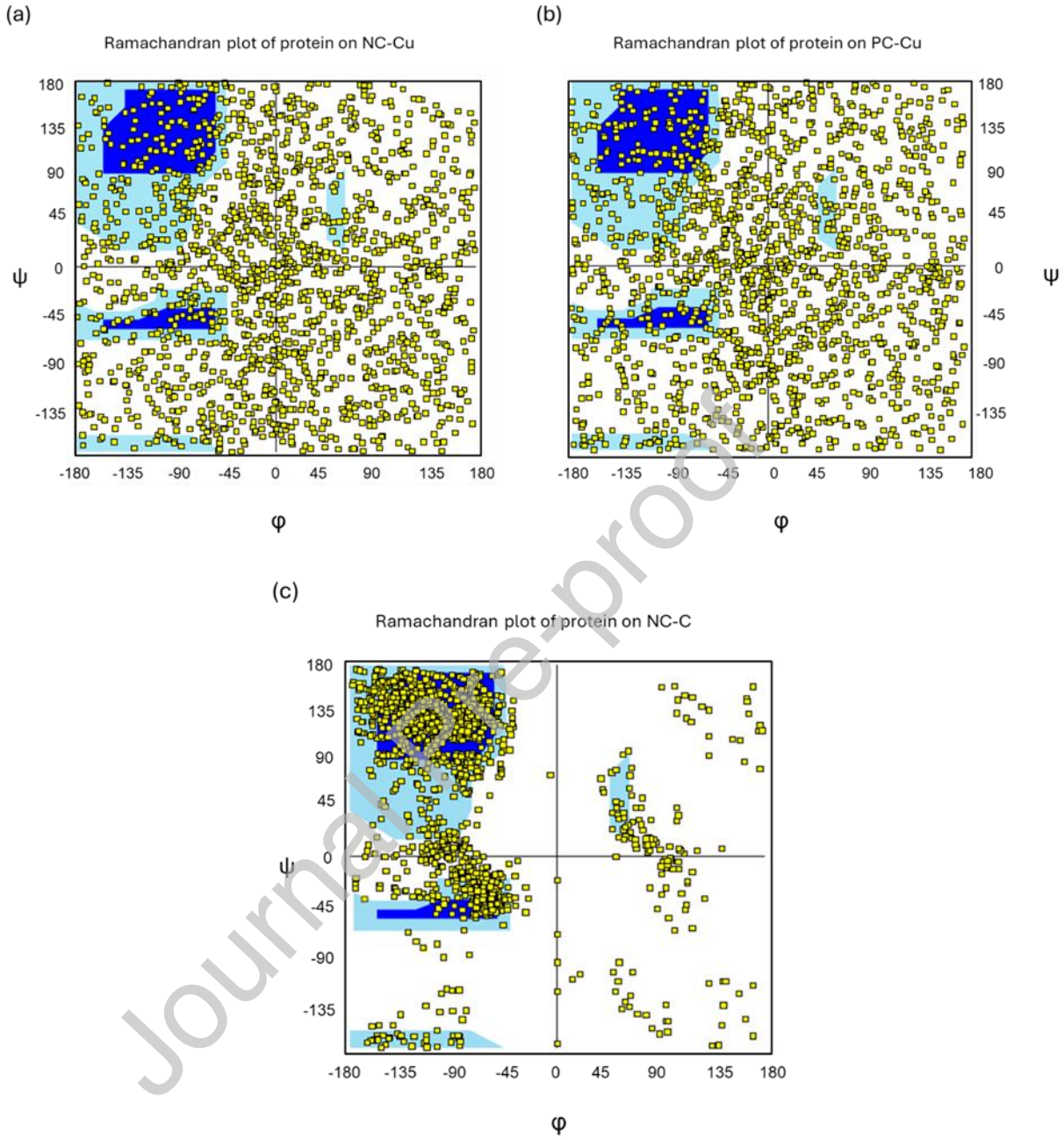

Fig. 15: Ramachandran plots of φ and ψ backbone dihedral angles for each substrate condition: (a) NC-Cu, (b) PC-Cu, (c) NC-C, (d) PC-C (provided in Supplementary Appendix D) and (e) aC (provided in Supplementary Appendix D). Yellow dots are sample torsion angles over the simulation time. Dark blue areas indicate the most allowed conformational regions (regions with beta-sheet and alpha-helix types), light blue areas represent other allowed regions and white areas are disallowed regions. NC-Cu and PC-Cu show wider angular spread with more points outside allowed regions. In contrast, NC-C, PC-C, and aC show tighter clustering within allowed regions, indicating less deviation from typical secondary structure conformations.

The presence of residues in disallowed regions of the Ramachandran plot has been shown in previous studies to correlate with protein's backbone destabilisation [49, 50].

Conversely, the NC-C, PC-C and aC environments showed a more limited clustering of φ and ψ angle within allowed conformational regions, see Fig. 15(c) and Fig. 15(d)

(provided in Supplementary Appendix D). These residues largely remained within the boundaries of the α-helix and β-sheet regions, which is characteristic of torsional stability and preserved structural integrity. Among these environments, the aC conformation, Fig.15(e) (provided in Supplementary Appendix D), showed the most compact distribution of angles, which is indicative of little conformational strain.

The findings here support the structural trends identified across all previous analyses. In particular, the broader distribution of residues into disallowed regions for NC-Cu and PC-Cu, indicates that these substrates are responsible for an increase in torsional strain, which leads to destabilisation of the backbone geometry. In contrast, the residues in the NC-C, PC-C and aC environments generally remain in the allowed conformational zones, reflecting stable torsional dynamics.

This outcome aligns with previous RMSF, displacement and dihedral angle results, showing carbon-based substrates responsible for native protein structure preservation and copper-based substates for inducing conformational disruption. The Ramachandran analysis therefore provides a final layer of structural validation, reinforcing the substrate-dependent effects on protein stability observed throughout the study.

4. Conclusion

Towards demystifying the antibacterial mechanisms, this study employed MD simulations to examine how substrate composition and granular structure influence the structural conformity of a bacterial protein through electrostatic charge transfer mechanics. By taking model examples of carbon and copper substrates, the work unravels intricate electrostatic charge transfer mechanics in an aqueous environment utilising REAXFF force field of MD. The findings address key questions often posed in literature and provide compelling mechanistic insights into early-stage molecular events governing antibacterial activity.

1. Substrate-dependent effects on protein conformation and interfacial electrostatics: While both NC-Cu and PC-Cu exhibit bactericidal activity, their underlying mechanisms of protein destabilisation diverge significantly. NC-Cu initiates a rapid, torsion-driven attack on the protein backbone, resulting in global structural destabilisation as shown by the high RMSD and Rg values and significant φ/ψ angle deviations concentrated within secondary structure regions. This behaviour is attributed to NC-Cu's uniform grain distribution, which applies consistent mechanical stress across the protein interface, triggering early-stage unfolding. In contrast, PC-Cu follows a more gradual and diffuse strategy. Its heterogeneous grain boundary architecture creates electrostatic gradients that induce sustained charge transfer into the protein, leading to residue-level instability. This is reflected in higher RMSF values, broader cumulative displacement, and moderate yet widespread ψ angle drift. These findings reveal two distinct attack strategies: NC-Cu acts as a fast, structurally invasive destabiliser targeting the protein backbone, whereas PC-

Cu operates through persistent, electrostatic destabilisation that weakens local residue integrity over time. This dual mechanism has been visually captured and summarised in Supplementary Appendix A. Carbon-based substrates, by comparison, showed minimal interaction strength, with reduced charge exchange and low structural impact. The protein retained its native geometry across all carbon surfaces, particularly aC, which exhibited the most neutral interface. This suggests a bacteriostatic profile, where weak charge interaction and low conformational disruption prevent denaturation while allowing structural preservation.

2. Early molecular deformations as indicators of antimicrobial action: The onset of structural destabilisation in copper environments emerged early during simulation, indicating a clear link between initial deformation and antimicrobial effect. NC-Cu caused immediate torsional destabilisation at the backbone, while PC-Cu induced gradual residue-level disruption through charge-driven stress. These temporally distinct responses both led to irreversible conformational changes, suggesting that early deformation serves as a reliable indicator of functional inactivation. By contrast, carbon substrates maintained stable protein structure throughout, showing no early signs of disruption, and thus consistent with a bacteriostatic mode of action.

3. Role of surface-induced charge distribution in protein disruption: Surface charge accumulation on copper substrates played a central role in destabilising protein structure, but the effect varied by substrate type. PC-Cu exhibited sustained and spatially uneven charge transfer, driven by grain boundary heterogeneity, which led to residue-specific structural fluctuations and cumulative displacement. In contrast, NC-Cu showed an early but less persistent charge response, suggesting a more mechanical, torsion-driven mode of disruption. These observations support the hypothesis that interfacial charge dipole interactions, particularly in polarisable environments, can trigger distinct patterns of structural rearrangement. This effect was evident under the ReaxFF potential, which captures the dynamic interplay between local charge distribution and conformational destabilisation.

4. Substrate-specific conformational integrity from dihedral and Ramachandran analysis: Dihedral angle analysis revealed substrate-dependent patterns of conformational disruption. NC-Cu induced sharp and persistent deviations in ψ angles, particularly within residues 100–107 and 330–374, which align with structurally critical domains previously identified in displacement analysis. This suggests localised backbone destabilisation driven by torsional strain. PC-Cu, by contrast, showed broader but less severe ψ angle shifts, consistent with more diffuse residue-level flexibility rather than complete unfolding. Ramachandran plots supported these trends: copper substrates prompted migration into disallowed φ/ψ regions, with NC-Cu showing the most significant deviation from canonical geometry. In contrast, carbon-based substrates —

especially aC preserved regular dihedral distributions within allowed regions, maintaining overall structural integrity and confirming their limited disruptive effect.

Acknowledgements:

SG would like to acknowledge the funding support from UKRI via Grant No. EP/T024607/1.

Conflict of interest:

Authors declare having no conflict of interest.

Declaration of generative AI and AI-assisted technologies in the writing process

During the preparation of this work, the author(s) used AI assistance to improve the readability and language of the manuscript. The authors reviewed and edited the final content and take full responsibility for the content of the published article.

Data statement:

Video files of the simulation results are provided as supplementary data (S1-S6).

Reference

1. Otter, J.A., S. Yezli, and G.L. French, *The role played by contaminated surfaces in the transmission of nosocomial pathogens.* Infection Control and Hospital Epidemiology, 2011. **32**(7): p. 687-699.
2. Hall-Stoodley, L., J.W. Costerton, and P. Stoodley, *Bacterial biofilms: from the natural environment to infectious diseases.* Nature Reviews Microbiology, 2004. **2**(2): p. 95-108.
3. Ajulo, S. and Awosile, B., *Global antimicrobial resistance and use surveillance system (GLASS 2022): investigating the relationship between antimicrobial resistance and antimicrobial consumption data across the participating countries.* PLoS One, 2024. **19**(2): p. e0297921.
4. McDonnell, G. and A.D. Russell, *Antiseptics and disinfectants: activity, action, and resistance.* Clinical Microbiology Reviews, 1999. **12**(1): p. 147-179.
5. Maillard, J.Y., *Resistance of Bacteria to Biocides.* Microbiology spectrum 2018. **6**(2): p. 10-128.
6. Ogunsona, Emmanuel O., Rajendran Muthuraj, Ewomazino Ojogbo, Oscar Valerio, and Tizazu H. Mekonnen, *Engineered nanomaterials for antimicrobial applications: A review.* Applied Materials Today, 2020. **18**: p. 100473.
7. Grass, G., C. Rensing, and M. Solioz, *Metallic copper as an antimicrobial surface.* Applied and Environmental Microbiology, 2011. **77**(5): p. 1541-1547.
8. Rai, M.K., Deshmukh, S.D., Ingle, A.P., Gade, A.K., *Silver nanoparticles: the powerful nano-weapon against multidrug-resistant bacteria.* Journal of Applied Microbiology, 2012. **112**(5): p. 841-852.
9. Warnes, S.L. and C.W. Keevil, *Mechanism of copper surface toxicity in vancomycin-resistant enterococci following wet or dry surface contact.* Applied and Environmental Microbiology, 2011. **77**(17): p. 6049-6059.

10. Santo, C. E., Lam, E. W., Elowsky, C. G., Quaranta, D., Domaille, D. W., Chang, C. J., & Grass, G., *Bacterial killing by dry metallic copper surfaces.* Applied and Environmental Microbiology, 2011. **77**(3): p. 794-802.
11. Vincent, M., Duval, R. E., Hartemann, P., & Engels-Deutsch, M., *Contact killing and antimicrobial properties of copper.* Applied and Environmental Microbiology, 2018. **124**(5): p. 1032-1046.
12. Liu, S., Zeng, T.H., Hofmann, M., Burcombe, E., Wei, J., Jiang, R., Kong, J. and Chen, Y., *Antibacterial Activity of Graphite, Graphite Oxide, Graphene Oxide, and Reduced Graphene Oxide: Membrane and Oxidative Stress.* ACS Nano, 2011. **5**(9): p. 6971-6980.
13. Perreault, F., A. Fonseca de Faria, and M. Elimelech, *Environmental applications of graphene-based nanomaterials.* Chemical Society Reviews, 2015. **44**(16): p. 5861-5896.
14. Hu, W., Peng, C., Luo, W., Lv, M., Li, X., Li, D., Huang, Q. and Fan, C., *Graphene-Based Antibacterial Paper.* ACS Nano, 2010. **4**(7): p. 4317-4323.
15. Li, W.R., et al., *Antibacterial activity and mechanism of silver nanoparticles on Escherichia coli.* Appl Microbiol Biotechnol, 2010. **85**(4): p. 1115-22.
16. Nanda, S.S., D.K. Yi, and K. Kim, *Study of antibacterial mechanism of graphene oxide using Raman spectroscopy.* Scientific Reports, 2016. **6**(1): p. 28443.
17. Latour, R.A., *Perspectives on the simulation of protein–surface interactions using empirical force field methods.* Colloids and Surfaces B: Biointerfaces, 2014. **124**: p. 25-37.
18. Liao, C., Li, Y. and Tjong, S.C, *Bactericidal and Cytotoxic Properties of Silver Nanoparticles. International journal of molecular sciences,* 2019. **20**(2): p. 449.
19. Gangadoo, S., Xu, C., Cozzolino, D., Latham, K., Della Gaspera, E., Chapman, J. and Truong, V.K., *Probing Nanoscale Interactions of Antimicrobial Zinc Oxide Quantum Dots on Bacterial and Fungal Cell Surfaces. Advanced Materials Interfaces,* 2022. **9**(3): p. 2101484.
20. Robinson, G. M., Tonks, K. M., Thorn, R. M., Reynolds, D. M., *Application of bacterial bioluminescence to assess the efficacy of fast-acting biocides.* Antimicrobial Agents and Chemotherapy, 2011. **55**(11): p. 5214-5220.
21. Sinha, R.P. and D.P. Häder, *UV-induced DNA damage and repair: a review.* Photochemical & Photobiological Sciences, 2002. **1**(4): p. 225-236.
22. Kreve, S. and A.C.D. Reis, *Bacterial adhesion to biomaterials: What regulates this attachment? A review.* Japanese Dental Science Review, 2021. **57**: p. 85-96.
23. Mücksch, C. and H.M. Urbassek, *Accelerated Molecular Dynamics Study of the Effects of Surface Hydrophilicity on Protein Adsorption.* Langmuir, 2016. **32**(36): p. 9156-9162.
24. Karplus, M. and J.A. McCammon, *Molecular dynamics simulations of biomolecules.* Nature Structural Biology, 2002. **9**(9): p. 646-652.
25. Amadei, A., A.B. Linssen, and H.J. Berendsen, *Essential dynamics of proteins.* Proteins, 1993. **17**(4): p. 412-425.
26. Ramachandran, G.N., C. Ramakrishnan, and V. Sasisekharan, *Stereochemistry of polypeptide chain configurations.* Journal of Molecular Biology, 1963. **7**: p. 95-99.
27. Goel, S., Kovalchenko, A., Stukowski, A. and Cross, G., *Influence of microstructure on the cutting behaviour of silicon.* Acta Materialia, 2016. **105**: p. 464-478.

28. Nair, M.R., Khaitan, A., Owhal, A., Chandra, I.R., Belgamwar, S.U., Mishra, R.R., Goel, S. and Roy, T., *A close-packed sphere model for characterising porous networks in atomistic simulations and its application in energy storage and conversion.* Carbon, 2024. **225**: p. 119089.
29. Iadanza, M.G., Higgins, A.J., Schiffrin, B., Calabrese, A.N., Brockwell, D.J., Ashcroft, A.E., Radford, S.E. and Ranson, N.A.., et al., *Lateral opening in the intact β-barrel assembly machinery captured by cryo-EM.* Nature Communications, 2016. **7**(1): p. 12865.
30. Jorgensen, W.L., Chandrasekhar, J., Madura, J.D., Impey, R.W. and Klein, M.L.., *Comparison of simple potential functions for simulating liquid water.* The Journal of Chemical Physics, 1983. **79**(2): p. 926-935.
31. Monti, S., C. Li, and V. Carravetta, *Reactive Dynamics Simulation of Monolayer and Multilayer Adsorption of Glycine on Cu(110).* The Journal of Physical Chemistry C, 2013. **117**(10): p. 5221-5228.
32. Thompson, A.P., Aktulga, H.M., Berger, R., Bolintineanu, D.S., Brown, W.M., Crozier, P.S., In't Veld, P.J., Kohlmeyer, A., Moore, S.G., Nguyen, T.D. and Shan, R., *LAMMPS - a flexible simulation tool for particle-based materials modeling at the atomic, meso, and continuum scales.* Computer Physics Communications, 2022. **271**: p. 108171.
33. Szakálos, Peter., Hultquist, Gunnar., Wikmark, G., *Corrosion of copper by water.* 2007. **10**(11): p. C63.
34. Lemire, J.A., J.J. Harrison, and R.J.J.N.R.M. Turner, *Antimicrobial activity of metals: mechanisms, molecular targets and applications.* 2013. **11**(6): p. 371-384.
35. Ding, F., S.V. Buldyrev, and N.V.J.B.j. Dokholyan, *Folding Trp-cage to NMR resolution native structure using a coarse-grained protein model.* 2005. **88**(1): p. 147-155.
36. Manandhar, S., Sankhe, R., Priya, K., Hari, G., Kumar B, H., Mehta, C.H., Nayak, U.Y. and Pai, K.S.R., *Molecular dynamics and structure-based virtual screening and identification of natural compounds as Wnt signaling modulators: possible therapeutics for Alzheimer's disease.* Molecular Diversity, 2022. **26**(5): p. 2793-2811.
37. Lindorff-Larsen, K., Maragakis, P., Piana, S., Eastwood, M.P., Dror, R.O. and Shaw, D.E., *Systematic validation of protein force fields against experimental data. PloS one*, 2012. **7**(2): p. e32131.
38. Lobanov, M., N. Bogatyreva, and O. Galzitskaya, *Radius of gyration is indicator of compactness of protein structure.* Molekuliarnaia biologiia, 2008. **42**: p. 701-706.
39. Glyakina, A.V. and O.V. Galzitskaya, *How Quickly Do Proteins Fold and Unfold, and What Structural Parameters Correlate with These Values?* Biomolecules, 2020. **10**(2).
40. Hassan, A.M., Gattan, H.S., Faizo, A.A., Alruhaili, M.H., Alharbi, A.S., Bajrai, L.H., Al-Zahrani, I.A., Dwivedi, V.D. and Azhar, E.I., *Evaluating the Binding Potential and Stability of Drug-like Compounds with the Monkeypox Virus VP39 Protein Using Molecular Dynamics Simulations and Free Energy Analysis. Pharmaceutical,* 2024. **17**(12): p. 1617.
41. Petrescu, A.J., Calmettes, P., Durand, D., Receveur, V. and Smith, J.C., *Change in backbone torsion angle distribution on protein folding.* Protein *Science*, 2000. **9**(6): p. 1129-1136.

42. Palmisano, V.F., *A metadynamics study of simple peptide chains*. (Doctoral dissertation), 2021.
43. Adhikari, A.N., K.F. Freed, and T.R.J.P.o.t.N.A.o.S. Sosnick, *De novo prediction of protein folding pathways and structure using the principle of sequential stabilization.* Proceedings of the National Academy of Sciences, 2012. **109**(43): p. 17442-17447.
44. Jung, S., *The Fastest Simulation of Protein Folding Based on Torsion Angles.* Journal of Bioinformatics and Systems Biology, 2021. **04**.
45. Hollingsworth, S.A. and P.A. Karplus, *A fresh look at the Ramachandran plot and the occurrence of standard structures in proteins. Biomolecular concepts,* 2010. *1*(3-4), p.271.
46. Wlodawer, Alexander., *Stereochemistry and validation of macromolecular structures.* Protein Crystallography: Methods Protocols, 2017: p. 595-610.
47. Sims, G.E. and Kim, S.H., *A method for evaluating the structural quality of protein models by using higher-order φ–ψ pairs scoring. Proceedings of the National Academy of Sciences*, 2006. **103**(12): p. 4428-4432.
48. Mani, H., Chang, C.C., Hsu, H.J., Yang, C.H., Yen, J.H. and Liou, J.W., *Comparison, Analysis, and Molecular Dynamics Simulations of Structures of a Viral Protein Modeled Using Various Computational Tools. Bioengineering*, 2023. **10**(9): p. 1004.
49. Mansouri, A., Yousef, M.S., Kowsar, R. and Miyamoto, A., *Homology Modeling, Molecular Dynamics Simulation, and Prediction of Bovine TLR2 Heterodimerization. International Journal of Molecular Sciences*, 2024. **25**(3): p. 1496.
50. Pal, D. and P. Chakrabarti, *On residues in the disallowed region of the Ramachandran map.* Biopolymers, 2002. **63**(3): p. 195-206.

Graphical Abstract

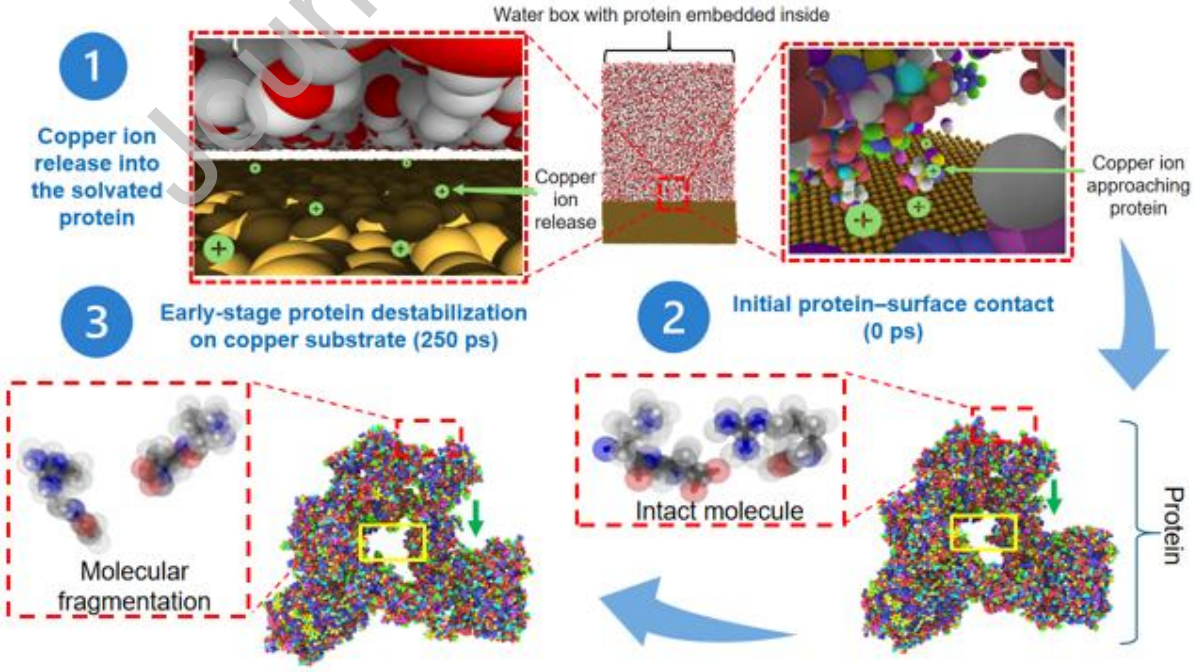

Statement of Significance

This study provides atomistic evidence of how copper and carbon surfaces differ in their early antibacterial behaviour. Reactive molecular dynamics (ReaxFF) simulations of five substrates (NC-Cu, PC-Cu, NC-C, PC-C and aC) interacting with the BamABCDE protein show that copper, especially nanocrystalline Cu induces rapid backbone torsional strain, elevated RMSD and Rg, and large residue displacements, indicating early-stage unfolding. Carbon surfaces, particularly amorphous carbon, maintain low RMSD and stable φ/ψ conformations. Copper also exhibits strong early charge accumulation (~0.2 C), whereas carbon remains nearly neutral. These substrate-dependent early perturbations distinguish bactericidal (Cu) from bacteriostatic (C) behaviour and provide mechanistic insight for designing next-generation antimicrobial coatings.

Declaration of Interest Statement

☒ The authors declare that they have no known competing financial interests or personal relationships that could have appeared to influence the work reported in this paper.

☐ The author is an Editorial Board Member/Editor-in-Chief/Associate Editor/Guest Editor for this journal and was not involved in the editorial review or the decision to publish this article.

☐ The authors declare the following financial interests/personal relationships which may be considered as potential competing interests: